Detachment folding, fold amplification, and diapirism in thrust wedge experiments

Marco Bonini

Istituto di Geoscienze e Georisorse, Sezione di Firenze, Consiglio Nazionale delle Ricerche, Florence, Italy

Received 19 September 2002; revised 22 April 2003; accepted 12 June 2003; published 20 November 2003.

[1] The relations between detachment folding, fold amplification, and salt diapirism in contractional settings have been investigated by means of scaled analogue models. The viscosity of the silicone layer simulating salt in nature and the shortening rates were combined in order to reproduce weak (type 1 models) and strong (type 2 models) décollements. Deformation patterns in the roof sequence exhibited two contrasting styles, (1) outward propagation of detachment folding along the décollement (OFP mode) and (2) passive roof duplex (PRD mode). In type 2 models, detachment folding propagated away from the most external thrust in the floor sequence, while in type 1 models, long-lived detachment folds almost invariably localized amplified above a floor thrust tip as a result of strain localization. A silicone wall intruded occasionally into the crestal graben of detachment folds in type 1 and OFP models. Best fitting of transition models data points indicates nonlinear relations with regression curves close to the equilateral hyperbola equation for both OFP-PRD and amplified detachment folds-box folds transitions. A quantitative comparison of model results with nature has been attempted by plotting salt-based fold-and-thrust belts data points on the scaled transition curves obtained from the modeling. Such a comparison relates shear stress products and ratios to the conditions favoring the amplification of detachment folds and the potential emplacement of ductile diapirs in their core. By reducing the roof sequence strength, pore fluid pressure λ_b is inferred to shift the equilibrium of fold-and-thrust belts toward the field of OFP and diapirism. *INDEX TERMS:* 8102 Tectonophysics: Continental contractional orogenic belts; 8005 Structural Geology: Folds and folding; 8010 Structural Geology: Fractures and faults; 8020 Structural Geology: Mechanics; 8045 Structural Geology: Role of fluids; *KEYWORDS:* fold-and-thrust belts, analogue modeling, salt tectonics, detachment folding, fold amplification, passive roof duplexes. **Citation:** Bonini, M., Detachment folding, fold amplification, and diapirism in thrust wedge experiments, *Tectonics*, *22*(6), 1065, doi:10.1029/2002TC001458, 2003.

0278-7407/03/2002TC001458$12.00

1. Introduction and Aims of the Work

[2] Anticlines developing in detachment (décollement) folding [*Blay et al.*, 1977; *Jamison*, 1987] require the presence of a basal décollement, where viscous material collect and infill the space generated in the core of the fold. In particular, detachment folding develops in the brittle hanging wall to accommodate the displacement of a bedding-parallel blind thrust along a lower ductile unit composed of salt or other evaporites (or overpressured shale). Accumulation of ductile material in the fold core may evolve to diapirism that therefore may accompany the fold development. The close coincidence of diapiric structures with anticlinal cores has been indeed recognized for a long time (see for instance the so-called "injection folds" of *Beloussov* [1959]).

[3] Recently, kinematic modeling of detachment folding has received great attention [e.g., *Homza and Wallace*, 1995; *Poblet and McClay*, 1996] and advanced models incorporating the geometries of syntectonic sediments in relation to fold growth have also been formulated [e.g., *Poblet and Hardy*, 1995; *Vergés et al.*, 1996; *Poblet et al.*, 1997]. However, the relations between detachment folding and diapirism have not received comparable consideration so far.

[4] In general terms, a diapir is when a viscous material pierces an overlying brittle overburden with discordant contacts. This contrasts with salt pillow and salt-cored anticlines that display concordant contacts between salt and overlying brittle strata. Brittle overburdens exceeding a critical thickness can be sufficiently strong to be impenetrable to salt diapirs [*Vendeville and Jackson*, 1992a]. However, faulting and erosion of the brittle overburdens are efficient mechanisms that locally reduce the overburden thickness, thus promoting diapirism and piercing. As a result, *Jackson and Vendeville* [1994] proposed that regional thin-skinned extension (or "reactive" diapirism) was the chief initiator of salt diapirism. Nevertheless, examples of salt diapirs developed in response to lateral shortening have also been reported [e.g., *O'Brien*, 1957; *Schwerdtner*, 1986; *Koyi*, 1988; *Talbot et al.*, 1988; *Velaj et al.*, 1999]. The present paper aims to investigate the conditions favoring the amplification of detachment folds and the development of diapiric structures under the influence of horizontal compression. To this purpose, a set of small-scale physical models was performed at the "Tectonic Modelling Laboratory" of the CNR-IGG, settled at the Earth Science Department of Firenze.

2. Analogue Modeling

[5] The mechanical behavior and evolution of fold-and-thrust belts have been extensively and profitably investigated

Table 1. Scaling Parameters[a]

Parameter	Model (Det.Fd.78; type 1)	Nature	Model/Nature Ratio
BL volumetric mass ρ_b, kg m^{-3}	1350	2400[b]	0.56
VL volumetric mass ρ_d, kg m^{-3}	1060	2200[b]	0.48
VL viscosity η, Pa s	7×10^2	3.3×10^{17}[b]	2.1×10^{-15}
BL internal friction coefficient μ	$\approx$0.6	0.6–0.85[b]	
BL cohesion c, Pa	80	40×10^6[b]	2×10^{-6}
BL/VL thickness ratio δ	0.5–5	0.3–30[b]	
Length l, m	0.01	3000	3.3×10^{-6}
Gravity acceleration g, m s^{-2}	9.81	9.81	1
Stress σ, Pa	53	2.9×10^6	1.9×10^{-6}
Strain rate ε, s^{-1}	10^{-4}	1.1×10^{-13}	$\varepsilon^* = \sigma^*/\eta^* = 9 \times 10^8$
Time t, s	3600	3.6×10^{12} ($\approx$0.11 Ma)	$t^* = (\varepsilon^*)^{-1} = 10^{-9}$
Rate of displacement v, m s^{-1}	4.7×10^{-7}	1.2×10^{-10} ($\approx$3.8 mm yr^{-1})	$v^* = l^*/t^* = 3.3 \times 10^3$
Rate of sedimentation s, m s^{-1}	2.3×10^{-7}	7×10^{-11} ($\approx$2.2 mm yr^{-1})	$s^* = l^*/t^* = 3.3 \times 10^3$

[a]The model to nature dimensionless ratios are indicated with an asterisk. BL, brittle layer (sand); VL, viscous layer (silicone).
[b]Parameters indicating average values.

by means of various analogue modeling techniques [e.g., *Davis et al.*, 1983; *Malavieille*, 1984; *Mulugeta and Koyi*, 1987; *Mulugeta*, 1988; *Colletta et al.*, 1991; *Davy and Cobbold*, 1991; *Liu et al.*, 1992; *Cobbold et al.*, 1993, 2001; *Burg et al.*, 1994; *Martinod and Davy*, 1994; *Gutscher et al.*, 1998; *Koyi et al.*, 2000; *Storti et al.*, 2000]. Salt diapirism has been explored employing layered brittle-ductile systems where the viscous layer is commonly simulated by silicone putty representing the source layer feeding the diapir. On the basis of model results, regional extension is thought to be the most efficient mechanism triggering diapirism [*Vendeville and Jackson*, 1992b; *Jackson and Vendeville*, 1994], while regional compression is generally found to oppose diapirism [e.g., *Vendeville*, 1991]. Diapirism may indeed develop only in particular contractional settings, such as when lateral compression follows an earliest stage of lateral extension [*Nilsen et al.*, 1995], in the case when there are lateral strength variation between the salt and its brittle overburden [*Cotton and Koyi*, 2000], tear faults cutting anticlines [*Vially et al.*, 1994], hinterland pinch out of décollement [*Costa and Vendeville*, 2001] and postshortening erosion of salt-cored anticlines [*Sans and Koyi*, 2001]. However, salt viscosity (η) should also represent an important parameter influencing salt diapirism. Although various viscosity contrasts between salt and its overburden have been taken into account in numerical model of diapirs [*Poliakov et al.*, 1996], as far as I know no analogue models have explored the influence of salt viscosity on detachment folding and diapirism developing in contractional settings. This paper intends therefore to explore this aspect, particularly the conditions that may lead to the emplacement of synshortening salt diapirs in the core of detachment folds.

2.1. Modeling Strategy and Scaling

[6] Analogue models were designed to simulate the vertical rheological layering associated with presence of a viscous salt layer within or beneath a brittle sedimentary cover overlying a crystalline basement. To represent a realistic small-scale replica of the prototype or natural process under investigation, the analogue models were scaled to nature following the principles of similitude [*Hubbert*, 1937; *Ramberg*, 1981; *Weijermars and Schmeling*, 1986] (Table 1). Models were designed assuming that 1 cm in the model represents 3 km in nature, implying the model to nature ratio of length l^* is 3.3 10^{-6} (Table 1). Dynamic similarity between model and natural prototype can be evaluated considering the Ramberg number that represents the ratio of gravitational force to viscous force acting on the viscous layer [*Ramberg*, 1981; *Weijermars and Schmeling*, 1986]. The Ramberg number is given as:

$$Rm = \frac{\rho_d g H_d}{\eta \dot{\varepsilon}} = \frac{\rho_d g H_d^2}{\eta v}, \quad (1)$$

where g is the gravitational acceleration, $\dot{\varepsilon}$ the strain rate, v the horizontal shortening velocity and ρ_d, η, H_d are volumetric mass, viscosity and thickness of the viscous layer.

[7] By reference to salt diapirism, natural fold-and-thrust belts underlain by salt exhibit two contrasting styles of deformation: 1) belts without significant diapirism and 2) belts with salt diapirism. In the first group, the salt décollement is inferred to be rather strong (similar to anhydrite) and diapirism is not developed, such as in Parry Island [*Harrison*, 1995a, 1995b] (Figure 1a). Fold-and-thrust belts of the other group instead exhibit significant diapirism and the salt is rather weak, as in the Zagros [*Talbot et al.*, 2000] and possibly in the Rif mountains [see *Yovanovitch*, 1922] (Figure 1b). Indeed, salt viscosity can vary over a wide range of values, from 10^{16} to 10^{20} Pa s [*Jackson and Talbot*, 1986; *Van Keken et al.*, 1993]. The importance of salt viscosity can be taken into account by considering the Ramberg number, *Rm*: the dynamic similarity of the model to nature can be evaluated assuming that both model and natural prototype share the same *Rm*, then, the bulk viscosity η_n of the natural décollement layer can be estimated using the experimental Ramberg number, Rm_{exp} [*Sokoutis et al.*, 2000]:

$$\eta_n = \frac{\rho_n g H_d^2}{v_n Rm_{exp}}. \quad (2)$$

The current modeling aimed to investigate the influence on deformation by décollement viscosity, therefore new models

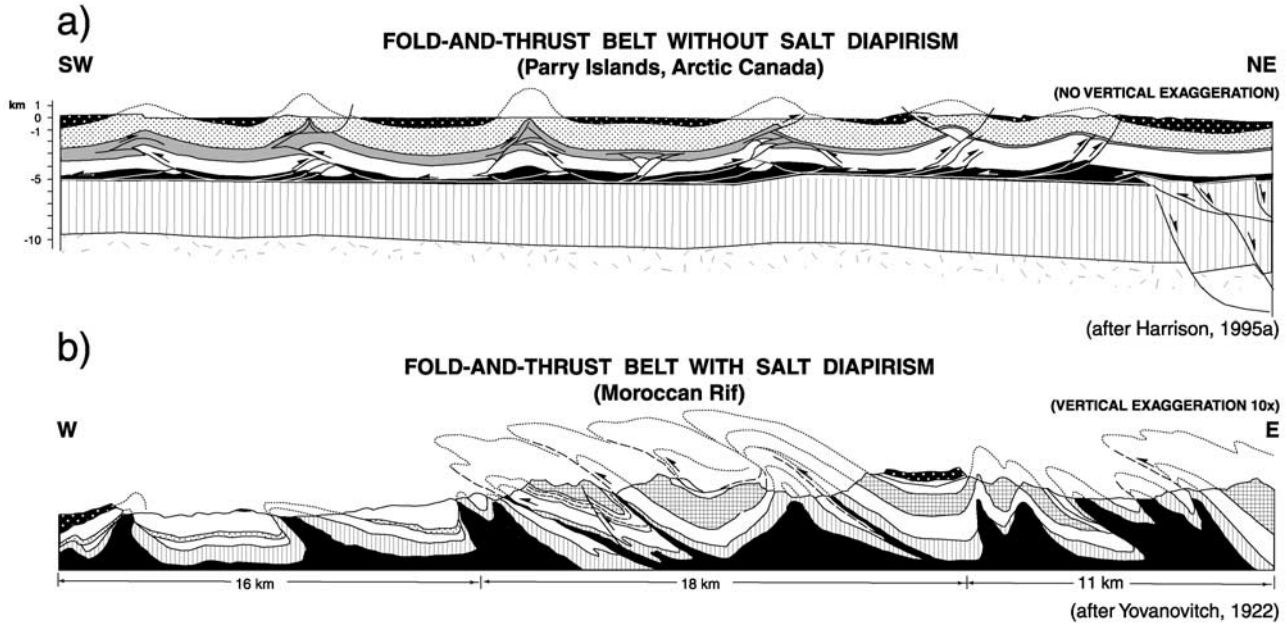

Figure 1. Transversal profiles exemplifying salt-based fold-and-thrust belts (a) without and (b) with salt diapirism. The salt layer is indicated in black. Figure 1a shows the Parry Islands, Arctic Canada (after *Harrison* [1995a], AAPG©1995, reprinted by permission of the AAPG whose permission is required for further use); Figure 1b shows the Moroccan Rif (after *Yovanovitch* [1922], reprinted by kind permission of the Société Géologique de France).

with a low-viscosity décollement (type 1 models) are compared with the results of previous models (mostly reported by *Bonini* [2001]) with a more viscous décollement (type 2 models) made of SGM 36 (PDMS) silicone polymer. For the chosen length ratio ($l^* = 3.3\ 10^{-6}$), from equation (2) the type 2 model viscosity of $5\ 10^4$ Pa s [*Weijermars*, 1986] scales to a natural bulk viscosity of the order of 10^{19}–10^{20} Pa s, which falls in the upper part of the viscosity field of salt. The weak type 1 décollement layer had instead a dynamic shear viscosity of about $7\ 10^2$ Pa s (see following section 2.2 for details), i.e., nearly two orders of magnitude lower than PDMS. From equation (1) (with parameters $\rho_d = 1060$ kg m^{-3}, $g = 9.81$ m s^{-2}, $H_d = 0.4$ cm, $\eta \approx 7\ 10^2$, shortening rate $v = 1.5$ cm h^{-1} and $= 0.15$ cm h^{-1} and corresponding strain rate $\dot{\varepsilon}$ varying from 10^{-3} s^{-1} to 10^{-4} s^{-1}; see section 2.2 and Table 2), type 1 models yielded values of $Rm_{exp} = 59.4$ and 594.2, respectively. Then, applying equation (2), and assuming $\rho_n = 2200$ kg m^{-3} (for salt), $H_d = 1200$ m (obtained from $l^* = 3.3\ 10^{-6}$), $g = 9.81$ m s^{-2} and an average velocity of shortening $v = 5$ mm yr^{-1}, the type 1 model décollement scales to a natural bulk viscosity of $\eta_n = 3.3\ 10^{18}$ Pa s (for $Rm_{exp} = 59.4$) and $\eta_n = 3.3\ 10^{17}$ Pa s (for $Rm_{exp} = 594.2$). Considering the velocity of shortening of 10–12 mm yr^{-1} over the Hormuz salt [*Hessami*, 2002] and the Holocene shortening of 26 mm yr^{-1} reported for the Zagros fold-and-thrust belt by *Vita-Finzi* [1986], the type 1 model décollement scales to a viscosity η_n of the order of 10^{16}–10^{18} Pa s, which is in good agreement with computation of salt viscosity obtained by *Talbot et al.* [2000] from extrusion rates of salt fountains in Iran. Therefore the chosen model setup allows a test of the role of décollement viscosity on deformation patterns of roof sequences deformed by detachment folding.

2.2. Model Deformation and Analogue Materials

[8] Previous analogue studies have demonstrated that the brittle and viscous behaviors of rocks can be successfully modeled using sand to represent the brittle layers and silicone putty to simulate the viscous layers (see *Brun* [1999] for a review). We then investigated the deformation under horizontal compression of a brittle-ductile system consisting of a viscous décollement layer (silicone putty) embedded between two frictional layers (sand), with the upper brittle layer representing a roof sequence (or the whole sedimentary cover) and the lower a floor sequence (or crystalline basement) (Figure 2).

[9] Models were built in a Plexiglas squeeze box (internal dimensions 24 cm × 10 cm × 10 cm) and had a length of 18 cm, width 10 cm and total thickness varying from 1.6 cm to 2.4 cm depending on the experiment (details of experiments are given in Table 2). Models were shortened by driving a rigid vertical wall into the sand-silicone pack at two distinct constant rates of convergence of 0.15 and 1.5 cm h^{-1}, respectively (Figure 2). For comparison all models were shortened up to 18–19% bulk shortening, though in specific models the bulk shortening value was eventually increased or reduced (Table 2). Lateral and top view photographs of the models were taken at constant time intervals during deformation. After deformation, models were covered with dry white sand to protect the final topography, and then soaked in water and frozen to allow

Table 2. Analogue Models Parameters[a]

Model	H_b, cm	H_d, cm	v, cm h^{-1}	τ_b, Pa	τ_d, Pa	$\dot{\gamma}_d$, s^{-1}	H_b/H_d	Figure Reference
Type I, Décollement Viscosity $\eta \approx 7 \times 10^2$ Pa s								
Det.Fd.60	0.2	0.4	0.15	96	0.07	10^{-4}	0.5	Figures 3a, 13a
Det.Fd.79	0.4	0.4	0.15	112	0.07	10^{-4}	1	Figures 3b, 5, 6a
Det.Fd.66[b]	0.4	0.4	0.15	112	0.07	10^{-4}	1	Figures 8i–8o
Det.Fd.78[b]	0.4	0.4	0.15	112	0.07	10^{-4}	1	Figures 8a–8g, 12d
Det.Fd.80[c]	0.4	0.4	0.15	112	0.07	10^{-4}	1	
Det.Fd.74	0.6	0.4	0.15	128	0.07	10^{-4}	1.5	Figures 3c, 6c, 13a
Det.Fd.77[d]	0.5–0.8	0.4	0.15	112	0.07	10^{-4}	1	Figure 11
Det.Fd.76	1	0.4	0.15	160	0.07	10^{-4}	2.5	Figure 3d
Det.Fd.62	0.2	0.4	1.5	96	0.73	10^{-3}	0.5	
Det.Fd.61	0.4	0.4	1.5	112	0.73	10^{-3}	1	
Det.Fd.69	0.6	0.4	1.5	128	0.73	10^{-3}	1.5	Figure 13a
Det.Fd.75	1	0.4	1.5	160	0.73	10^{-3}	2.5	
Type 2, Décollement Viscosity $\eta = 5 \times 10^4$ Pa s								
Det.Fd.43	0.2	0.4	0.3	96	10	2.1×10^{-4}	0.5	Figures 3e, 13a
Det.Fd.45	0.4	0.4	0.3	112	10	2.1×10^{-4}	1	Figures 3f, 4a
Det.Fd.47	0.6	0.4	0.3	128	10	2.1×10^{-4}	1.5	Figure 3g
Det.Fd.50	1	0.4	0.3	160	10	2.1×10^{-4}	2.5	Figure 3h
Det.Fd.35	0.2	0.4	1.5	96	52	10^{-3}	0.5	
Det.Fd.67[c]	0.2	0.4	1.5	96	52	10^{-3}	0.5	Figure A1b
Det.Fd.17	0.4	0.4	1.5	112	52	10^{-3}	1	Figure 4b
Det.Fd.40	0.6	0.4	1.5	128	52	10^{-3}	1.5	
Det.Fd.33	1	0.4	1.5	160	52	10^{-3}	2.5	
Det.Fd.81[e]	1	0.4	1.5	160	52	10^{-3}	2.5	Figure A1a

[a]Type 2 models (except models Det.Fd.67 and 81) are from *Bonini* [2001]. Models deformed to 18–19% bulk shortening (BS).
[b]Models deformed with synshortening sedimentation.
[c]Models deformed up to 28% BS.
[d]Models deformed with lateral variation in thickness H_b.
[e]Models deformed to 5% BS.

cutting of longitudinal sections without disturbing the model.

[10] The brittle layers were simulated using dry quartz sand, a Mohr-Coulomb material with a volumetric mass of $\rho_b = 1350$ kg m^{-3}, angle of internal friction $\varphi \approx 31°$ ($\mu \approx 0.6$), and cohesion $c \approx 80$ Pa. The thickness H_b of the upper brittle layer varied from 0.2 cm to 1 cm depending on the experiment, while the thickness of the lower brittle layer was 1 cm in all experiments.

[11] The thickness H_d of the viscous layer was 0.4 cm, so that the H_b/H_d ratio ranged from 0.5 to 5 (Table 2). The low-viscosity décollement layer (type 1 models) was simulated by silicone putty obtained by mixing to homogeneity "Mastic Silicone Rebondissant 29" (provided by CRC Industries, France) and Oleic acid in the proportion of 4:1 (by weight). Laboratory tests on this material indicate a Newtonian behavior with a dynamic shear viscosity $\eta \approx 7\ 10^2$ Pa s (at $26 \pm 2°$C) and volumetric mass $\rho_d = 1060$ kg m^{-3}, implying a

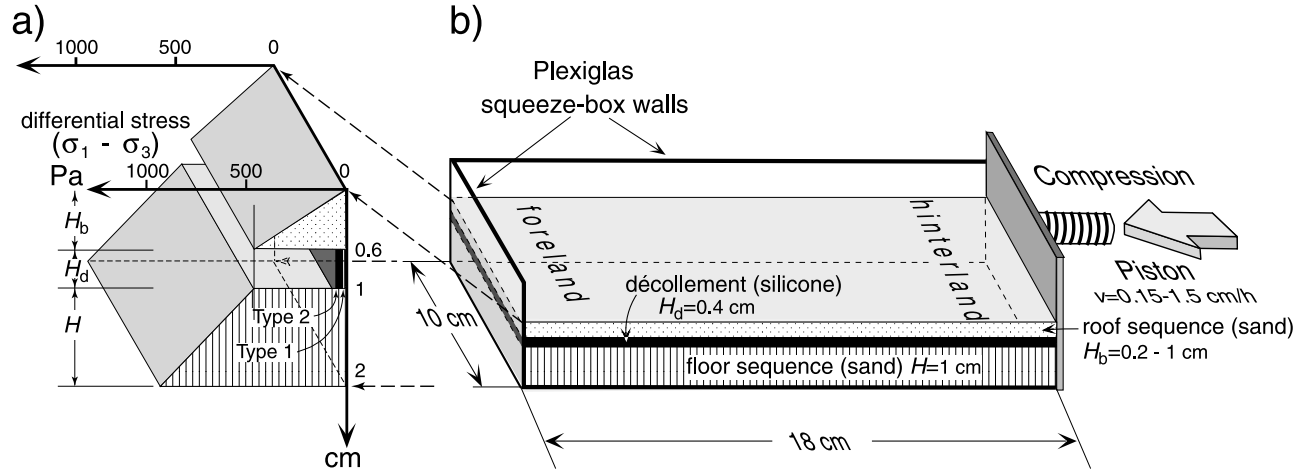

Figure 2. Simplified sketch showing (a) the model strength profile and (b) the model setup. The strength profile is referred to models Det.Fd.69 (type 1) and Det.Fd.40 (type 2).

density contrast (ρ_b/ρ_d) $\approx$ 1.27. To visualize strain, the type 1 décollement layer was made up of alternated rectangles of silicone with different color. The stronger silicone PDMS (type 2 models) was deformed in such a way that even the faster strain rate was sufficiently low to fall in the field of Newtonian behavior [*Weijermars*, 1986], emphasizing its viscous component with respect to the elastic component [*Ten Grotenhuis et al.*, 2002].

[12] The shear stress in the viscous layers is estimated assuming that deformation in the model décollement layer is near simple shear (Couette flow) at the onset of shortening. Newton's equation stating that the shear stress is directly proportional to the strain rate (under streamlined conditions) is then applicable [e.g., *Collyer*, 1973; *Weijermars*, 1997]:

$$\tau_d = \eta\dot{\gamma}_d = \eta\left(\frac{v}{H_d}\right), \tag{3}$$

where τ_d is the shear stress acting on the viscous layer, η the dynamic viscosity and $\dot{\gamma}_d$ the engineering shear strain rate, which is given by the ratio between the velocity v applied to the upper plate and the thickness of the viscous layer H_d. The engineering shear strain rate $\dot{\gamma}_d$ is generally used as an approximation for experiments in which deformation in viscous layers is near simple shear ($\dot{\gamma}_d \approx \dot{\varepsilon}_m$) [e.g., *Brun*, 1999], both in compressional and extensional settings [e.g., *Nalpas and Brun*, 1993; *Faccenna et al.*, 1999]. This approximation is in agreement with structural analyses carried out along salt décollements in which deformation is mostly simple shear (e.g., Pyrenees [*Sans et al.*, 1996]). Although model deformation appears to be more complex, this approach for calculating model strain rates has also been used in this paper (Appendix A and Table 2) approximating v to the velocity of horizontal compression and taking H_d as the initial viscous layer thickness, since simple shear is mostly accommodated by strain and flow over the entire thickness of the viscous layer (section 3 and Appendix A).

2.3. Limitations of Modeling

[13] The floor sequence was laid directly above the rigid base of the Plexiglas squeezebox, thus no sort of isostatic compensation was possible in the modeling. This configuration resulted in an inflexible floor sequence instead of a flexible one, and also in an exaggerated topographic relief. This adopted model configuration is certainly more appropriated to the cases where the floor sequence is assumed to represent a rigid basement (see section 2.1). Erosion and synshortening sedimentation were not normally included in the modeling procedure, even though numerical [*Poliakov et al.*, 1993, 1996] and analogue [*Sans and Koyi*, 2001] models demonstrate they play a fundamental role in salt diapirism. However, a few models investigated the role of sedimentation and the eventual spontaneous collapse of fold crests that reduced the local roof thickness. Furthermore, no effects related to dissolution or hydratation of salt have been considered.

[14] Another potential source of limitations is represented by the small dimensions of the squeeze box that may raise the possibility that sidewall friction may affect model results. Perhaps, the lateral friction may have caused the wedge to be shorter than it would be in case of no lateral friction. However, this paper was mainly concerned on the differences in the deformation styles of thrust wedges depending on the shear stresses in roof sequence–décollement systems. The good correspondence and systematic distribution of the structural styles exhibited by the models in relation to the shears stresses (see below sections 3 and 4) indicates that the results of this experimental study are reliable.

3. Patterns of Model Deformation

[15] Previous analogue work on thrust wedges explored the geometry of deformation of a system composed of a viscous décollement embedded between an upper brittle roof sequence and a lower brittle floor sequence [*Bonini*, 2001]. Depending on both the brittle strength of the roof sequence and the viscous strength of the underlying décollement, deformation of the roof sequence resulted into two distinct styles: outward folding propagation (OFP, dominated by detachment folding) and a passive roof duplex (PRD [*Banks and Warburton*, 1986]). Generally, the OFP style developed for $H_b/H_d \leq 2$ and PRD style when $H_b/H_d \geq 2.5$; PRD and OFP were separated by a transition field.

[16] Figure 3 illustrates two representative series of cross sections (with each series composed of four models) corresponding to models simulating weak (type 1; Figures 3a–3d) and strong (type 2; Figures 3e–3h) salt décollement. In each series, the thickness of the roof sequence H_b was varied while keeping the strain rate constant ($\dot{\gamma}_d \approx 10^{-4}$ s^{-1} for type 1 and $\dot{\gamma}_d \approx 2.1\ 10^{-4}$ s^{-1} for type 2); consequently, the décollement strength τ_d of models shown in Figure 3 was of the order of 0.07 Pa and 10 Pa in type 1 and 2, respectively (Table 2).

[17] Deformation style of both type 1 and 2 models exhibit typical features, such as imbricate foreland-verging thrust faults (linked by a basal floor thrust) in the floor sequence close to the moving wall and various patterns of folding and deformation in the roof sequence that are accompanied by horizontal and vertical displacements in the silicone. The geometry of the thrusts sheet array in the floor sequence is referred to as a "floor duplex" when they are bounded by both a basal floor thrust and by a passive roof thrust. A floor duplex therefore differ from a "floor imbricate fan" where the thrust sheets are bounded only by a floor thrust (see Figures 2 and 3 for terminology of structures) [e.g., *McClay*, 1992, and references therein]. Thrust faults in the floor sequence regularly turned into shear zones and flattened as they propagated into the décollement, giving rise to various deformation styles depending on the strength of both the roof sequence and the décollement layer.

3.1. Deformation Patterns in the Roof Sequence

[18] Analysis of model cross sections allows the distinction of two main features in the deformation patterns of roof sequences: (1) the roof sequence is predominantly affected by mostly symmetric detachment folds nucleated in the décollement layer and (2) the roof sequence is decoupled

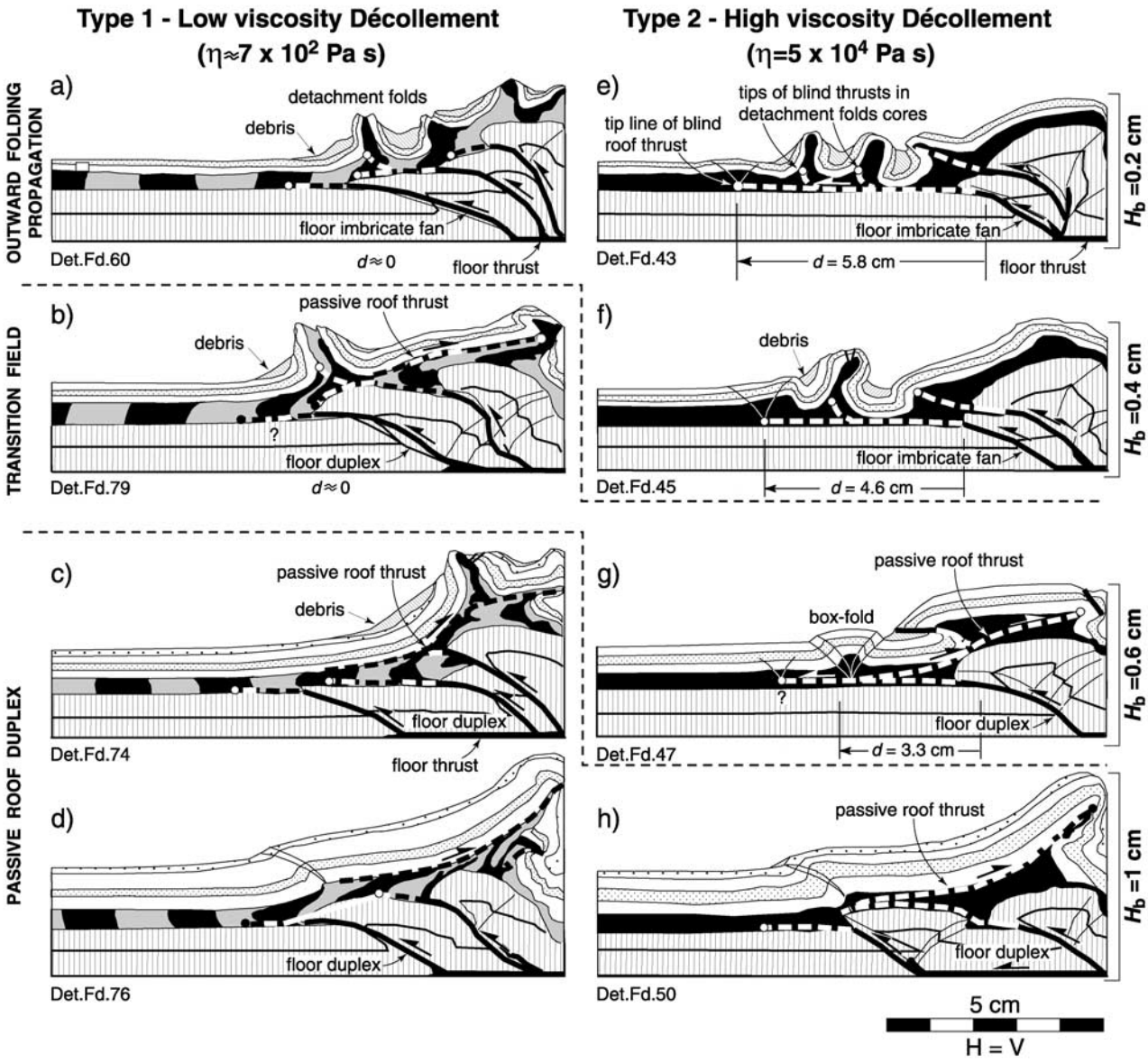

Figure 3. Line drawings of models with (left) low-viscosity (type 1) and (right) high-viscosity (type 2) silicone that scale to weak and strong natural salt décollement of the order of 10^{16}–10^{18} Pa s and 10^{19}–10^{20} Pa s, respectively. In each series, (a, e, and f) outward folding propagation, (b and g) transition field, and (c, d, and h) passive roof duplex, models were deformed with constant $\dot{\gamma}_d$ and varying H_b. Dashed lines indicate the hypothesized shear zones in the décollement layer.

hinterlandward (along the décollement) above the floor duplex (Figure 3). This latter deformation style is generally associated with a foreland-dipping monocline and is consistent with the passive roof duplex (PRD) geometry [*Banks and Warburton*, 1986], which is substantially equivalent to the concept of "triangle zone" of *Gordy et al.* [1977] and *Price* [1981].

[19] The number, geometry and distribution of detachment folds in the roof sequence vary depending upon H_b, H_d and τ_d (Figure 3). Generally, the number of detachment folds is inversely proportional to the roof sequence thickness, i.e., the number of folds increases with decreasing H_b (Figure 3). This observation agrees with the analytical solution and analogue studies of periodic instabilities developing in a brittle-ductile system under compression [*Martinod and Davy*, 1994].

[20] The geometries of detachment folds clearly relate to both H_b and τ_d. In type 2 models, an increase in H_b (with $H_b \geq 0.4$ cm) and τ_d favor the box fold geometry. Conversely, for thin roof sequences (H_b = 0.2–0.4 cm), detachment folds generally amplify by folding mechanisms involving limb lengthening and/or limb rotation (see sections 3.2 and 3.3). Analysis of models indicates that amplification of fold is favored by low τ_d. This dependence

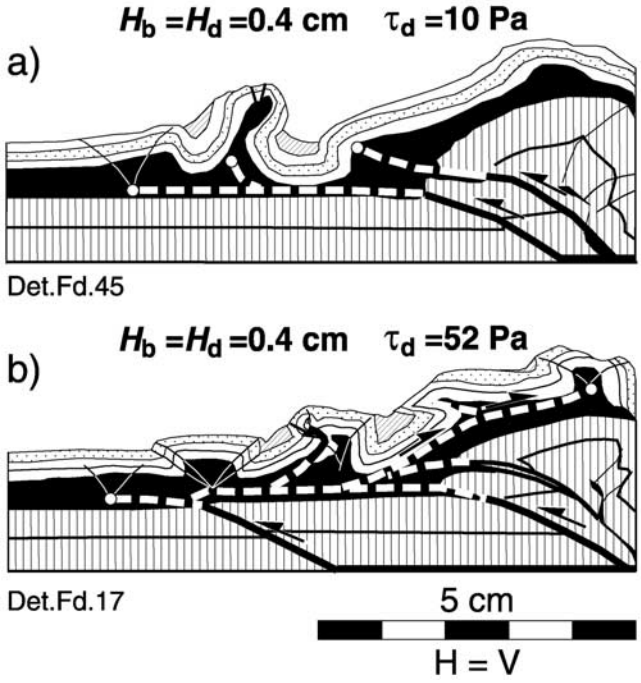

Figure 4. Effect of brittle-ductile coupling on geometry of detachment folds. Models (a) Det.Fd.45 and (b) Det.Fd.17 (from *Bonini* [2001]) were built with the same initial geometry but were deformed under different rates (Table 2). This resulted in an amplified and tightened detachment fold for the weaker décollement (Figure 4a) and characteristic box folding for the stronger one (Figure 4b).

is exemplified by comparison between model Det.Fd.45 and model Det.Fd.17 (Figure 4). Both models belong to the type 2 series and were built with $H_b = H_d = 0.4$ cm, but $\tau_d = 10$ Pa in model Det.Fd.45 and $\tau_d = 52$ Pa in model Det.Fd.17 (Table 2). This variation in the décollement strength resulted in a tightened detachment fold in model Det.Fd.45 (Figure 4a), whereas model Det.Fd.17 exhibited characteristic box folding (Figure 4b). The importance of τ_d on the mode of detachment folding is emphasized by type 1 models which exhibit amplified detachment folds up to relatively high H_b values (i.e., $H_b \leq 0.6$ cm). Notably, a characteristic feature of detachment folds developed in type 1 models is the surfacing of silicone in the fold core (Figures 3a–3c) displaying in some cases the characteristics of diapiric structures (see section 3.2). By contrast, the silicone PDMS is not normally exposed in folds cores in type 2 models, nor does it display clear features indicative of diapirism.

[21] Detachment folds differ significantly in their distribution in type 1 and type 2 models. In type 2 models, successive detachment folds develop and propagate increasing distance away from the floor imbricate fan (or floor duplex) whereas in type 1 they develop above or behind it (Figure 3). This is illustrated by the distance d between the most external detachment fold in the roof sequence and the corresponding thrust in the floor sequence. Whereas the value of d increases considerably with decreasing H_b in type 2 experiments (Figures 3e–3g), d is practically nil in type 1 models where the detachment fold develops directly above the tip of the floor thrust (Figures 3a and 3b). This suggests that, in some cases, a strong décollement layer may decouple structures in the roof sequence from those in floor sequence more efficiently than a weak décollement layer. Type 2 models can therefore be referred to a typical outward folding propagation style (OFP). Type 1 models exhibiting detachment folding as the chief deformation mechanism (Figure 3a) can be still included in the OFP field, though they are less efficient than type 2 models in transferring deformation outward along the décollement. The coexistence of a passive roof thrust with the development of a detachment fold at the front of the floor duplex has been treated as transition field (TR; Figures 3b and 3g).

[22] Following the approach adopted by *Nalpas and Brun* [1993] and *Brun and Nalpas* [1996] for extension, and *Bonini* [2001] for compression, model results are analyzed assuming that their deformation is controlled by mainly a combination of τ_b, the shear stress at the base of the roof sequence, and τ_d, the shear stress in the viscous layer (assuming simple shear deformation). Such shear stresses τ_b and τ_d have been estimated by using the Mohr-Coulomb equation (equation B1 in Appendix B) and equation (3), respectively. The shear stress τ_b has been calculated along the potential horizontal surface of detachment given by the interface between the brittle roof sequence and the viscous layer, where σ is the vertical normal stress (ρgh) counterbalancing the potential sliding along this surface (Table 2). Models reported in *Bonini* [2001] showed that a decrease in τ_d (thus a decrease in the brittle-ductile coupling for a fixed τ_b) resulted in an increase of distance d. However, the current type 1 models indicate that below a critical viscous strength the horizontal propagation of shear stress is inhibited and the distance d is zero. The importance of bulk shortening on horizontal propagation of deformation along the décollement has also been tested by increasing the amount of finite shortening (see Table 2). However, increasing bulk shortening did not increase the distance d.

3.2. Detachment Folds Amplification

[23] The results of analogue modeling have shown that thin roof sequences favor the amplification of detachment folds up to an extraordinary extent. The mechanism of folding can be inferred by analyzing sequential top view photos taken during the evolution of a typical detachment fold in models of the type 1 series. Model Det.Fd.79 (Figure 5) exemplifies the amplification of a slightly asymmetric long-lived foreland-verging detachment fold, which is flanked on both sides by open synclines. The anticline crest is broken by a graben that became more pronounced as the fold grew vertically. In accord with the experimental work by *Blay et al.* [1977], asymmetry developed late in the fold amplification process. A cross section (Figure 5e) shows the hinge of the external syncline to be rather sharp, while the hinge of the internal syncline is well rounded. The anticline forelimb (on the left) in Figure 5 is steep and slightly overturned; through time, the external syncline hinge approximately underlay the crest of the anticline forelimb (Figures 3b and 5). On this basis, as well as on

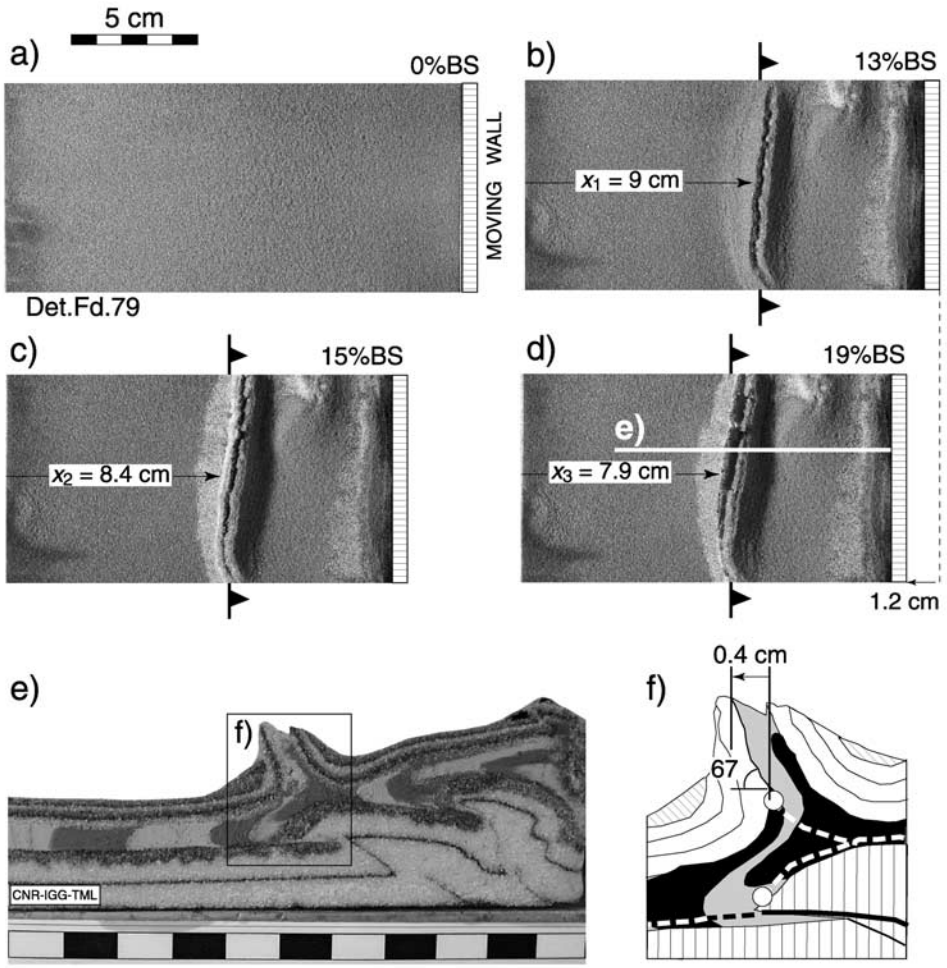

Figure 5. Sequential top view photographs of a growing detachment fold with development of the crestal graben in model Det.Fd.79. Distance of the external detachment fold forelimb to the end wall (distance x) nearly equals the forward displacement of the moving wall in the same time interval (Figures 5b–5d). This indicates the existence of a strong localization of deformation at the long-lasting fold structure. The higher uplift rate of the forelimb is denoted by the instability and large collapse of material. Overturning of the fold in Figure 5e is inferred to have occurred in late stages of fold development favored by the collapse of its ductile core. Estimate of the forelimb overturning is shown in Figure 5f.

the observation of cross sections cut at earlier stages of fold growth, the distance between the fixed end wall and the top of the anticline forelimb is taken as a measure of the rate of lateral hinge migration. This distance progressively decreased with shortening by about the same amount as the moving wall advanced (Figure 5), suggesting that the detachment-folding mechanism involves strain localization in the fold structure and also forelandward migration of the hinge of the outer syncline. Such a mechanism implies the presence of active axial surfaces during the progressive lengthening of both anticline limbs to amplify the folds [*Suppe et al.*, 1992]. The overturned forelimb (dipping $\sim 67^\circ$) may apparently contrast with this interpretation of outward migration of the fold, which could instead be merely due to rotation and overturning of the forelimb about a stationary hinge. However, the lateral migration, during advanced stages of growth of the fold, can be estimated to exceed 1.1 cm (Figures 5b–5d) whereas the overturning can be estimated to have produced about 0.4 cm of outward migration (Figure 5f). In addition, the same fold development (with distance of hinge migration close to the amount of bulk shortening produced in the same time interval) is frequently observed in upright folds (see for instance the external fold in model Det.Fd.60; Figure 3a). However, it is likely that also limb rotation may have contributed to the fold growth, especially in the early stages, though lateral hinge migration and limb lengthening would have been the dominant processes of fold amplification. Such a deformation style was favored by the strong decoupling along type 1 décollement, which had the effect of transferring portions of relatively undisturbed roof sequence into the forelimb of the anticline, in a similar fashion to

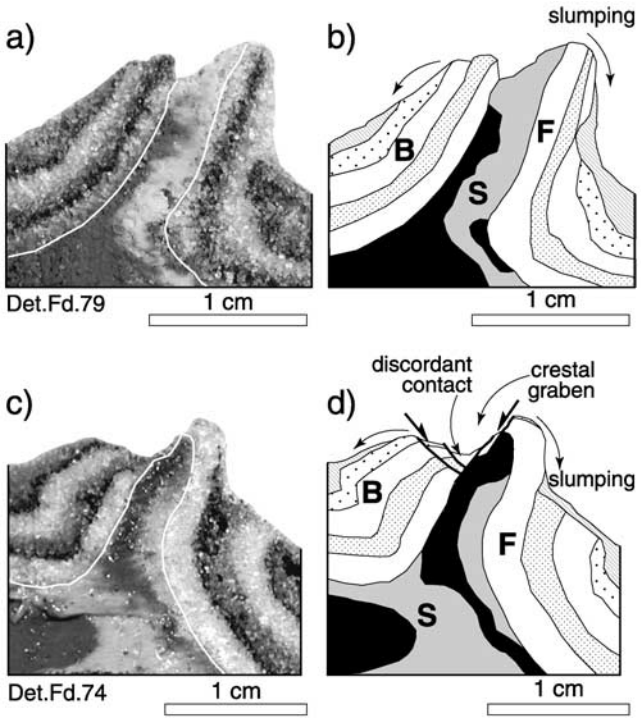

Figure 6. Close-up of detachment fold cores exemplifying the two main deformation patterns identified in type 1 models. (a) Photograph and (b) interpretative line drawing of a ductile wall exhibiting concordant contacts with both fold limbs. Note the sense of asymmetry of the top silicone free surface at the fold core pointing to a faster growth rate of the forelimb. (c) Photograph and (d) interpretative line drawing of a ductile wall exhibiting a disconformable contact with the broken fold hinge. B, backlimb; F, forelimb; S, silicone. The thin white lines indicate the boundary of the silicone. See color version of this figure at back of this issue.

thrust-related folds [e.g., *Tavarnelli*, 1993]. However, to better discriminate the mechanisms of fold amplification, particularly the contribution of limb rotation, some models were performed to incorporate the effect of syntectonic sedimentation that develops a record of the kinematics of fold limbs (see section 3.3).

[24] Limb lengthening and lateral hinge migration was accompanied by silicone rising in the anticline core, resulting in largely conformable structures similar to salt (ductile) walls (or ridges with cuspate crests) [*Jackson and Talbot*, 1994]. In type 1 models, the silicone was invariably exposed over the hinge of the folds crests (excepts for very thick cover; Det.Fd.76; Figure 3d) and in some case it even rose above the local topographic surface, suggesting a link with the mechanism of folding. Whereas in many cases the model "salt wall" was concordant with the anticline limbs and the anticline crest was completely missing (Figures 6a and 6b), in some others the ductile wall (together with the forelimb) rose out the anticline crest and was clearly discordant with the brittle cover in the fold hinge region (a feature that would be diagnostic of salt diapirism; Figures 6c and 6d). Notably, the rise of the forelimb and silicone illustrated in Figures 6c and 6d (see also sections 3.3 and 3.4) is consistent with the hypothesized predominant limb lengthening model.

[25] On the above evidence, detachment fold growth is here illustrated in terms of relative rates of activity by limb lengthening of axial surfaces. In the early stages of fold amplification, rates of limb lengthening and lateral hinge migration are similar for both limbs (Figure 7a). With

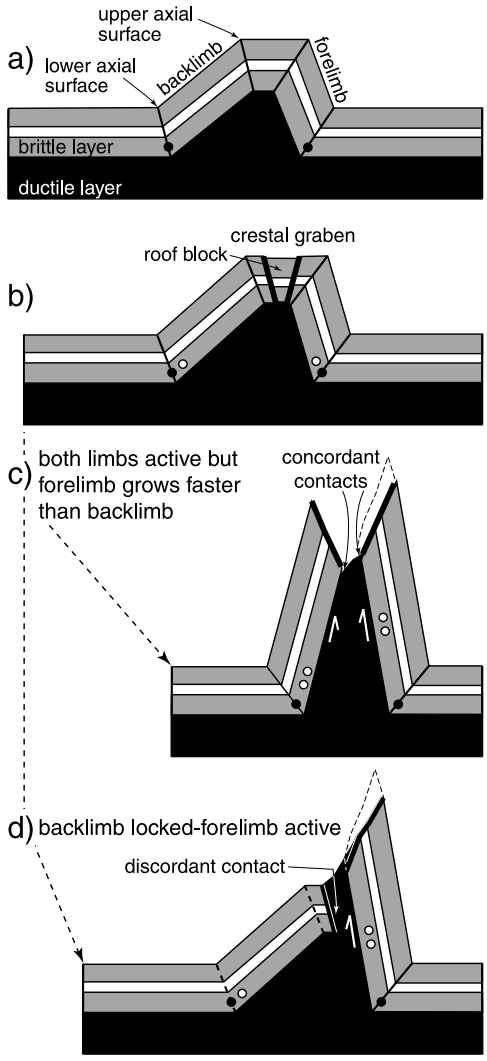

Figure 7. Schematic cartoon showing the inferred evolution of detachment folds. Concordant or discordant contacts between the ductile (silicone) wall and the fold limb(s) are interpreted in terms of competing rates of limb growth by lengthening. Solid and dashed lines indicate active and inactive axial surfaces, respectively. The roof block is missing in Figures 7c and 7d owing to slumping of the crest and straightening out the former crest of the anticline along the upper active hinge(s). Circles indicate the positions of particles passing through the axial surface (black and white circles represent the current and past positions of axial surfaces, respectively).

increased shortening, a graben forms over the anticline crest (Figure 7b). The development of such a ''crestal graben'' could be due to various mechanisms that may act together, such as (1) rising of silicone in the anticline core, (2) gravitational collapse of the fold crest above its ductile core, (3) outer arc extension (above the neutral surface) during anticlinal bending. Horizontal stretching is indeed observed above salt-cored anticlines [e.g., *Turner and Hancock*, 1990], as well as at the crest of natural and analog diapirs [e.g., *Dixon*, 1975; *Davison et al.*, 1993]. This step in the history of detachment folds has also been observed in type 2 models, but, with increasing deformation, types 1 and 2 models exhibit contrasting evolutionary paths. In type 2 models the detachment fold stop growing and deformation in the viscous layer is accommodated by the development of a new fold. In type 1 models, owing to the strong brittle-ductile decoupling, the deformation is instead localized much longer in the same fold. In addition, in type 1 models the graben formed over the fold crest since the early stages of growth of the fold, then, as the fold amplified, it evolved to a structure similar to a dilatational fissure. This may suggest that the gravity collapse would not play a major role in the early stages of fold growth, so that rise of silicone or outer arc extension would have initiated the crestal graben. Detachment folds in type 1 models may evolve in two different ways (Figures 7c and 7d):

[26] 1) When both anticline limbs are growing at similar rates the silicone wall displays conformable contacts to both fold limbs (Figure 7c). The roof block is normally missing so that the silicone is exposed at surface. The free surface of the silicone typically shows an asymmetric hinterlandward-dipping profile that indicates the forelimb grew faster than the backlimb (Figures 6a, 6b, and 7c). This may indicate that both lower and upper axial surfaces are active before, during, and after the crestal graben development. The absence of disconformable contacts and the observation that the silicone did not rise over the anticlines crest apparently exclude the contribution of diapirism to this process of fold amplification.

[27] 2) When lengthening of the anticline backlimb stops or decreases drastically (i.e., both upper and lower axial surfaces of the detachment fold backlimb are inactive) and the forelimb continue to lengthen, the ductile (silicone) wall invades the crestal graben (generally along its outer margin) and rises out of the fold crest exhibiting a sharp discordance with the backlimb (Figures 6c, 6d, and 7d). By contrast to the previous deformation style, this mode should involve the contribution of a sort of diapirism.

3.3. Models With Synshortening Sedimentation

[28] Previous analogue models have shown that thrust evolution can be significantly affected by syntectonic sedimentation [*Storti and McClay*, 1995; *Bonini*, 2001]. Removal by erosion of a large thickness of sediments from the zone of active uplift and their resedimentation in adjacent sedimentary basins represent an efficient mechanism that is able to redistribute an enormous volumes of deposits. This process can lead to significantly variations in the lithostatic stress within a fold-and-thrust belt. Major sediment accumulations in foreland basins suggest that the lithostatic loads generated by such syntectonic clastic wedges may effectively interfere with the propagation of active thrust fronts.

[29] In this work, a number of models with syntectonic sedimentation were performed to visualize the evolution of the fold geometry through time in order to discriminate between the potential mechanisms responsible for detachment folding. Following a well-tested technique, syntectonic sedimentation was simulated by sieving thin sand layers at regular time intervals into basins developing in a fold-and-thrust belt shortening at a steady rate. The effect of synshortening sedimentation on fold evolution is exemplified by models Det.Fd.66 and Det.Fd.78 (Figure 8), where local sedimentation started at 18% and 22% bulk shortening (BS), respectively, and localized to the sides of the most external growing detachment fold named hereafter the ''emergent anticline''. Sediments were deposited at about 45 min intervals (≈0.6% BS), but the bulk rate of accumulation may vary slightly from model to model because of the intrinsic difficulty in introducing an exact quantity of sand during each sedimentation event.

[30] The sedimentation rate in the model (s_m) can be scaled down to nature (s_n) by dividing the scaled thickness of the sedimentary wedge in the model ($l_n = l_m/l^*$) by the scaled time span of sedimentation ($t_n = t_m/t^*$):

$$s_n = \frac{l_m t^*}{t_m l^*}. \quad (4)$$

In model Det.Fd.78 (left-hand side of Figure 8), the maximum thickness of syntectonic sediments (time of sedimentation t_m = 585 min) is l_m = 8.5 mm (which scales down to a thickness in nature of l_n = 2575 m), while in model Det.Fd.66 (time of sedimentation t_m = 405 min) l_m = 6.6 mm (and l_n = 2000 m). From equation (4), sedimentation rates scale to s_n = 2.6 mm yr^{-1} and s_n = 2.3 mm yr^{-1} in models Det.Fd.66 and 78, respectively (see Tables 1 and 2 for modeling parameters), values representing fast sedimentation rates [e.g., *Suppe et al.*, 1992].

[31] Relations between growth strata geometry and fold kinematics have previously been related to two contrasting models: progressive limb rotation [*Riba*, 1976; *DeCelles et al.*, 1991; *Ford et al.*, 1997] versus kink band migration with instantaneous limb rotation [*Suppe et al.*, 1992, 1997]. These two mechanisms may act separately, even if both growth geometries have been documented as developing during the same time interval [*Zapata and Allmendinger*, 1996]. The kinematic history of detachment folds is discussed below on the basis of the growth strata architecture in terms of limb rotation, limb lengthening and fixed or active axial surfaces inferred from the longitudinal cross sections of models Detd.Fd.66 and 78 [e.g., *Poblet et al.*, 1997].

[32] The models can be easily compared to the setting of the external Pyrenees where, since the pioneering work of *Riba* [1976], the development histories of detachment folds bounding the foreland Ebro Basin are determined in the architecture of growth sediments. The diagrams in Figures 8h and 8p portray the length and dip of the forelimb

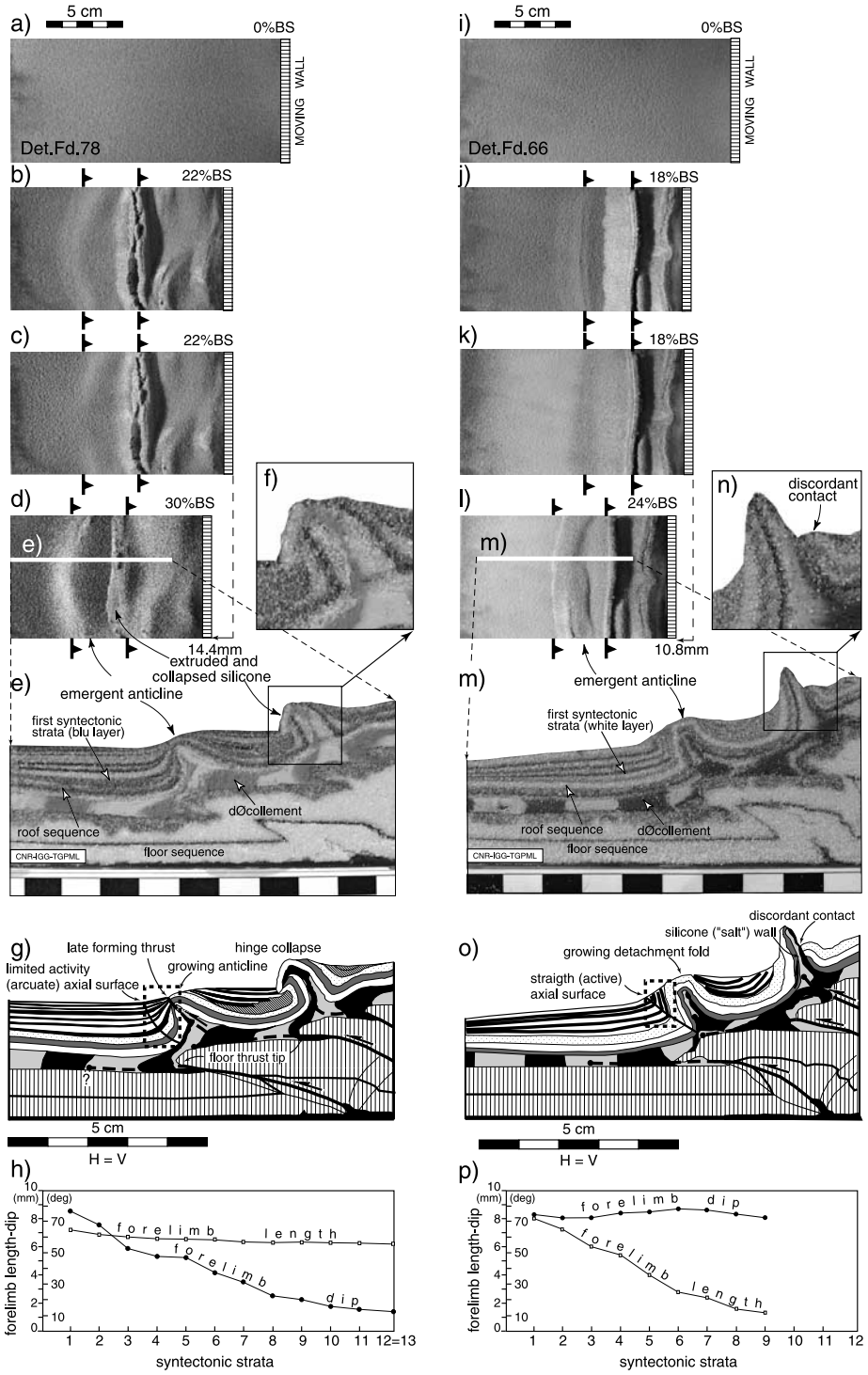

Figure 8. Models performed with synshortening sedimentation. Top view photographs illustrate the main experimental phases: (a, i) initial, (b, j) prior to sedimentation, (c, k) after the first sedimentation event, and (d, l) final topography. (e, m) Transversal sections and (g, o) corresponding line drawings show detachment folds located typically above floor thrusts tips. The black box in Figures 8e and 8m indicates the close-up of amplified detachment folds in Figures 8f and 8n. The dashed box in Figures 8g and 8o at the frontal part of the emergent anticline indicates were dip and length of syntectonic strata have been measured and reported in the diagrams of Figures 8h and 8p. Numbers in Figures 8h and 8p denote the growth strata from the lower to the upper. Black triangles indicate the position of the main blind floor thrusts tip. The thin white lines indicates the boundary of the silicone. See color version of this figure at back of this issue.

of the emergent anticline as recorded by the syntectonic cumulative wedge sedimented in front. In model Det.Fd.78, the growth strata recors a progressive decrease in the dip of the fold limb upsection and a rather constant limb length (Figure 8h), suggesting that this detachment fold evolved primarily by progressive rotation of the fore limb. In accord with the model proposed by *Meigs* [1997], the formation of a thrust fault displaced both prekinematic and synkinematic strata over the fold core after a substantial amount of rotating limb detachment folding (Figures 8e and 8g).

[33] In model Det.Fd.66 (right-hand side of Figure 8), the architecture of the growth strata instead displays progressive limb lengthening and rather constant limb dip, suggesting that the detachment fold evolved mainly by axial (kink band) migration (Figure 8p). In this mechanism, the syncline hinge migrated laterally forward for a distance approximately corresponding to the length of the lowermost folded syntectonic strata (strata 1 in Figures 8m and 8p). This length (≈8 mm) represents a large proportion of the horizontal bulk shortening (distance x = 10.8 mm in Figure 8), suggesting that the growth of the emergent anticline accommodated most of the bulk shortening occurring in that time interval (i.e., between steps k and l in Figure 8).

[34] The preliminary results obtained from the above models indicate that both progressive and instantaneous limb rotation are plausible mechanisms that may operate in models and in nature. Apparently, both the rate of sedimentation and cross-sectional area and tapering of the syntectonic sedimentary wedge may represent parameters controlling these two different fold growth mechanisms (compare Figure 8e with Figure 8m). As a first approximation, a predominant kink band migration model would be favored by a thinner clastic wedge with marked tapering, a fact which may accord with the hinge migration limb lengthening mechanism of fold amplification inferred for type 1 models with thin roof sequences (see section 3.2).

3.4. Strain Localization and Salt Diapirism

[35] Strain localization at detachment folds in type 1 models is induced by the low décollement viscosity and it is thought to markedly amplify the detachment folds. During fold amplification, in some cases the ductile wall may break and intrude the anticline hinge along a formed margin of the crestal graben (Figures 6c, 6d, and 8n). This suggests that the rise of the ductile wall in the core of the fold exerts an active push below the fold crest, in a similar fashion to an ''active diapir'', which is defined as a ductile diapir able to lift, deform and intrude the brittle overburden under the effect of buoyancy forces alone. However, the application of the force analysis of *Schultz-Ela et al.* [1993] to this context reveals the lack of any significant active component in the diapirism. This implies that other mechanisms of diapirism are necessarily acting in the system, most likely those associated with the above mentioned strain localization.

[36] An approach to estimate the minimum pressure generated by the rise of the ductile core is to consider the pressure necessary for a viscous fluid to intrude a preexisting fault or fracture, like those bounding the crestal graben (see evolution illustrated in Figure 7). The procedure used for this computation [e.g., *Acocella et al.*, 1999] equals the behavior of the weak salt analogous to that of other viscous fluids, such as magma (neglecting the effect of temperature). Considering uniaxial lithostatic conditions, the pressure P necessary to intrude a preexisting fracture is given as [*Jaeger and Cook*, 1979; *Delaney et al.*, 1986; *Acocella et al.*, 1999]:

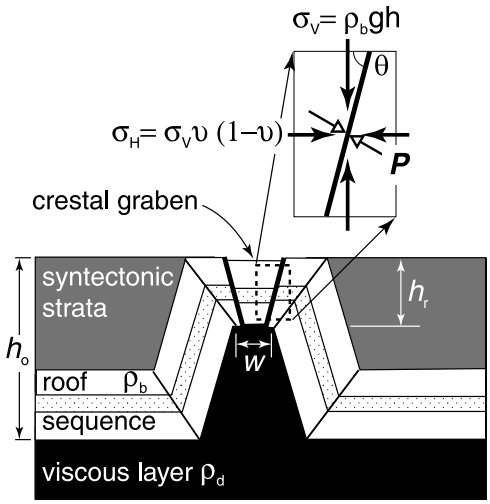

Figure 9. Schematic cartoon indicating the parameters used to estimate the minimum diapiric pressure generated at the detachment folds crest, below the crestal graben.

$$P = \frac{(\sigma_V + \sigma_H)}{2} - \cos 2(90^\circ - \theta)\frac{(\sigma_V - \sigma_H)}{2}, \qquad (5)$$

being $\sigma_V = \rho_b g h_r$ the vertical lithostatic stress, $\sigma_H = \sigma_V \upsilon/(1 - \upsilon)$ the horizontal lithostatic stress and υ the Poisson modulus (for sand, average value $\upsilon = 0.25$ in the work of *Storti et al.* [1997]). Considering average values observed in models with synshortening sedimentation (such as, $\theta \approx 75^\circ$, $h_r \approx 0.004$ m) it gives $P = 20$ Pa (see Figure 9 for symbols).

[37] The setting of many detachment folds of type 1 models (exemplified by Figures 6a and 6b) with conformable contacts and absence of extrusion does not allow to identify unambiguously the contribution of diapirism related to the active rise of the ductile core. However, the recognition of such a rise of the ductile core owing to the occasional inactivity of the backlimb (by promoting disconformable contacts), raises the possibility that a similar mechanism be active also when both limbs are growing at similar rates. This process may also explain the straight (and lengthy) fold limbs and the frequent disappearance of the roof block at the crest of type 1 models detachment folds (Figures 3a, 3b, 6a, and 6b). The active rise of the ductile core may have indeed straighten out the former crest of the anticline along a strain active hinge at the upper end of the limbs (upper axial surfaces; see evolution in Figures 7a–7c), thus also favoring the slumping off the topographic highs (fold limbs, roof

block and crest). In addition, this progression may have also favored the evolution of the crestal graben to a structure more similar to a dilatational fissure (Figures 6a and 6b).

[38] The current models highlight the importance of décollement viscosity and brittle-ductile coupling in controlling strain distribution. Strong décollements (type 2) favor the horizontal propagation of detachment folding, while weak décollements (type 1) favor the development of long-lived detachment folds showing marked vertical amplification and strain localization. Strain localization is presumably associated with lateral hinge migration and limb lengthening, during which the silicone is "pumped" into the fold core and intruded vertically above the tips of nominal blind ductile thrusts in the anticlinal cores, further favoring the fold amplification [e.g., *Turner and Hancock*, 1990]. This would promote stretching of fold crests and may possibly lead to the piercing and rising of the ductile wall out the broken fold hinge if the backlimb inactivates. In this case, the active forelimb may be viewed as a sort of passive roof thrust rising, together with the silicone wall, above the deactivated backlimb (Figures 3c, 6c, and 6d). The forelimb and ductile wall may lengthen and rise actively at an extraordinary extent above the broken fold hinge (see Figures 8j–8l and 8n) and become eventually unstable and collapse over the surface as exemplified in Figures 8g–8f.

[39] Although buoyancy forces may contribute to drive the silicone toward the anticlinal core, which represents the lowest pressure zone in the experimental system, the present work suggests that the main driving forces are provided by the tectonic "pumping". Following the term proposed by *Beloussov* [1959] for the laterally squeezed viscous mass opening the crests of anticlines, a suitable term describing these special cases of surface breaking structures or diapirs might be "injection walls" or, alternatively, "diapiric detachment folds".

4. Application of Model Results to Nature

4.1. Qualitative Comparison of Model Results With Natural Fold-and-Thrust Belts

[40] The results of modeling display most of the characteristics described for natural detachment folds and the architecture of their growth strata. If similarity conditions are satisfied, this good correspondence indicates a similarity in dynamic processes meaning that models can be used to understand better the mechanics of the geological processes considered. From a geometrical point of view, the silicone-cored detachment folds that amplified, tightened and in case pierced the crest of model folds (Figures 3–8) can be qualitatively compared with patterns known from field examples of detachment folds and salt diapirs. Any similar natural structure might also have developed as detachment folds growing from shallow to moderate detachments. Experimental results suggest that salt diapirism associated with detachment folding is unlikely to occur where the thickness of the model sedimentary cover exceeds 4–6 mm. However, natural salt diapirism is a complex process depending upon many factors, such as shear stress (τ_b, τ_d), erosion-sedimentation patterns, and pore fluid pressure conditions (λ) (see section 4.2 and Appendix B). Examples of amplified detachment folds and diapirism briefly discussed below include the External Hellenic Arc, the Pyrenees and the Zagros.

[41] The modeling results discussed above also offer the possibility of comparing the propagation of basement thrusts into the overlying sedimentary cover to the role played by the intervening viscous décollement. Models indicate that, for a roof sequence sufficiently thin to allow detachment folding, these relations are strongly dependent upon décollement strength. In the case of a relatively strong décollement, such as viscous salt or anhydrites (type 2 models), deformation should propagate outward, away from where the hangingwall of a thrust in the basement protrudes into the overlying viscous layer. Conversely, in the case of a weak décollement (type 1 models) detachment folds should approximately overlie the tips of basement thrust faults.

4.1.1. Detachment Folding in the External Hellenic Arc and the Pyrenees

[42] The northern Hellenic Arc, off the shore of Western Greece, is characterized by Triassic evaporites surfacing along the leading edges of thrust sheets. This evaporite unit acted as décollement and represents the source layer of Pliocene- Pliocene-Quaternary diapirs, that can be described in terms of vertical salt walls [*Underhill*, 1988]. The evaporites appears to initially risen through the shortened cover along thrust ramps and then risen vertically through the syn-shortening Pliocene-Quaternary deposits. Diapiric rise has been related to initial thrust sheet loading and subsequent diapiric growth accentuated by Pliocene-Quaternary subsidence and sedimentation [*Underhill*, 1988]. A close association between some of these diapirs with thrust faults is imaged in some seismic sections across this margin [*Monopolis and Bruneton*, 1982; *Auroux et al.*, 1984; *Brooks and Ferentinos*, 1984] (Figure 10). Both the structural position of these diapirs above a viscous décollement layer and their large vertical growth associated with relatively thin pre-kinematic strata raise the possibility that they evolved in a similar fashion to the detachment folds that formed in models with thin roof sequences (see Figures 3a–3b and 8). The patterns of extension suborthogonal to the diapiric margins described by *Underhill* [1988] are also comparable with the patterns observed in the models, where horizontal stretching affects the crest of the ductile core to the detachment fold.

[43] Typical salt-cored detachment folds are also well exposed in the Prepyrenean External Sierras bounding the foreland Ebro Basin [*Millán et al.*, 1994, 1995]. These folds exhibit many features diagnostic of detachment folding, particularly the marked fold amplification associated with collapsed hinge antiforms [*Millán et al.*, 1995; *Arenas et al.*, 2001]. Serial geological cross sections illustrate marked along-strike variations in style of detachment folds in the External Sierras [*Millán et al.*, 1995; *Arenas et al.*, 2001]. These characteristics are also well documented in the models; for instance, transverse sections across model Det.Fd.77 portray several of the structural details described in this field example, most notably, the lateral transition from large-scale hinge collapse to back-thrusting accommo-

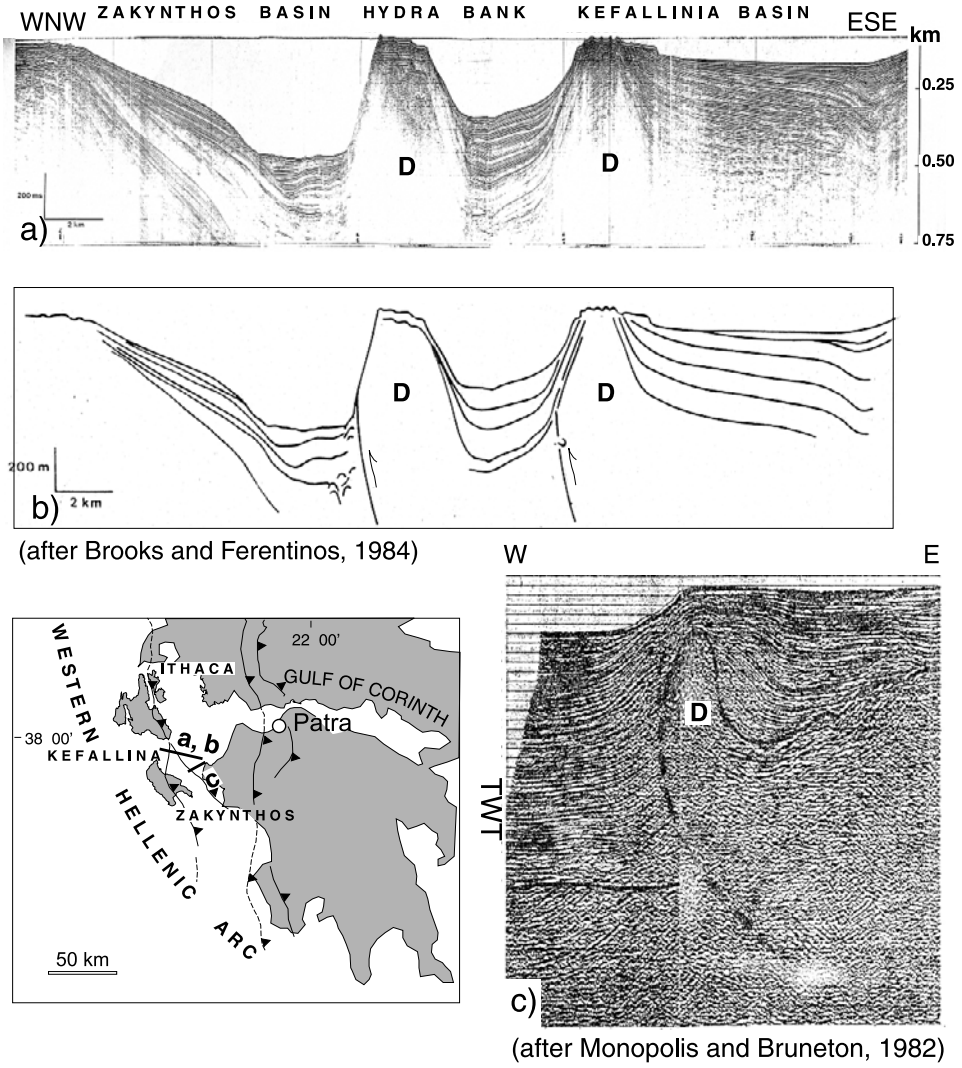

Figure 10. Seismic sections from the External Hellenides showing the association of reverse faulting with diapirism at detachment fold structures. Compare the vertical diapiric growth of the "salt walls" with the amplified detachment folds of models illustrated in Figures 3–8; D, salt diapir. Reprinted from *Brooks and Ferentinos* [1984] and *Monopolis and Bruneton* [1982], with permission from Elsevier.

dating deformation in the anticline crest region (Figure 11). On the basis of model deformation, hinge collapse in nature may be related to the continual vertical growth of the limb(s), so that, as the anticline amplifies, it becomes unstable and collapses under its own weight (Figure 11).

4.1.2. Salt Diapirism in the Zagros Fold-and-Thrust Belt

[44] The Zagros fold-and-thrust belt represents a classical area where both basement thrusts and salt diapirs occur together [e.g., *Farhoudi*, 1978; *Berberian*, 1995; *Edgell*, 1996]. The occurrence of two major décollement layers at different levels in different parts of the Zagros stratigraphy allows focus on the relations between diapirism and the strength of the roof sequence. The décollement layers, mainly composed of salt and anhydrites, correspond to the basal 1–1.5 km-thick Cambrian Hormuz salt [*Kent*, 1970] and to the upper Miocene Fars Group, with an original thickness estimated at 1.2-1.8 km [*O'Brien*, 1957]. These thicknesses indicate that the model silicone layer 4 mm thick simulates these décollement. Both salt layers gave rise to spectacular diapiris [*O'Brien*, 1957; *Ala*, 1974], but the styles of modes of rise from each layer appear to be conceptually very different. The Hormuz salt was overlain by a 6- to 7-km-thick roof sequence (the Competent group of *Colman-Sadd* [1978]), which, according to model results, would have been impenetrable to salt diapirs. As a matter of fact, the vigorous diapiric activity of Hormuz salt has been attributed to either thin or thick-skinned extension long before the Zagros orogeny [*Jackson and Vendeville*, 1994], and/or the rise of salt up pull-apart-like basins developed along oblique footwall ramps reactivating during the Zagros orogeny above older transfer zones and associated salt pillows [*Talbot and Alavi*, 1996]. Conversely, shortening of the Fars salt and anhydrites (Lower Fars in

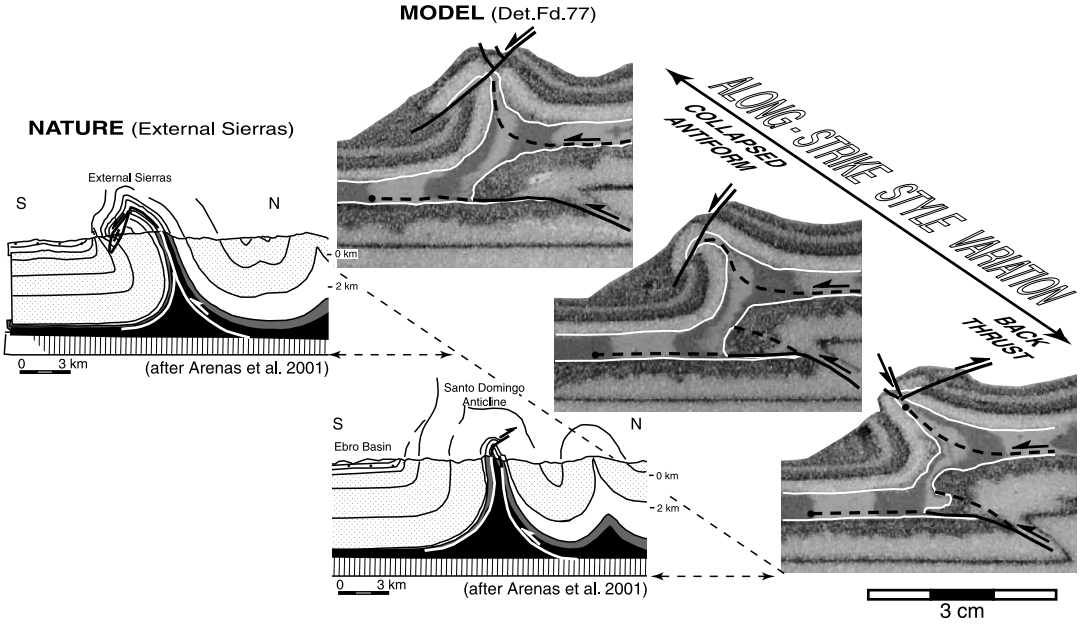

Figure 11. Comparison between characteristics of natural detachment folds in the External Sierras (a, b; simplified from the original work by *Millán et al.* [1995] in *Arenas et al.* [2001], reprinted by permission of the Sociedad Geológica de España) and transversal sections in model Det.Fd.77, where lengthening and uplift of the forelimb was accompanied by relevant collapse. Note the good correspondence of structural details between models profiles and the natural examples. The thin white lines indicates the boundary of the silicone.

O'Brien [1957]) started with an overlying sedimentary cover (Middle Fars plus Upper Fars) only about 900 m thick [*O'Brien*, 1957]. This deformation resulted in the development of salt pillows which evolved to salt-cored anticlines which tightened as deformation progressed. Sedimentation of synshortening Pliocene marls and sandstones (Bakhtiari Group) reached thicknesses of about 3 km in the adjacent synclines [*O'Brien*, 1957] (Figures 12a and 12b). By the end of deformation, the salt typically pierced the fold cores and was exposed at the surface (Figure 12c) resulting in deformation profiles similar to those inferred from models built with a comparable initial geometry. The deformation pattern in Figure 12c has been drawn on the basis of the model results, with nominal ductile thrusts in the salt layer emanated from thrusts affecting the underlying floor sequence (compare Figure 12c with Figure 12d as well as with models in Figures 3a–3b, 6, and 8m–8o).

[45] In summary, salt diapirism in the Zagros illustrates how the thickness of the roof sequence above the ductile layer exerts a primary control on salt piercement and upwelling in a fold-and-thrust belt. Whereas the thick and strong roof sequence impeded the rise of the Hormuz salt and mechanisms other than pure compression have been advocated for diapirism (i.e., extension or pull-apart-like openings), a thinner (and therefore weaker) roof sequence was easily pierced by salt diapirs along the cores of detachment folds in Late Miocene-Pliocene times. These observations agree with the current and previous [e.g., *Jackson and Vendeville*, 1994] modeling results which highlight the major role played by the strengths of roof sequence and the décollement in controlling deformation patterns and salt diapirism. Nevertheless, an apparent discrepancy between model results and nature is that the Zagros is commonly described as typical fold-and-thrust belt with OFP style, while modeling suggests that the great thickness of the sedimentary sequence above the Hormuz salt should instead favor the development of passive roof duplexes. Either such passive roof duplexes exist and have not yet been recognized, or their absence should be reexamined critically.

4.2. Quantitative Comparison of Model Results With Natural Fold-and-Thrust Belts

[46] The dynamic scaling of the models described here is generally sufficiently realistic for the model results to allow near-quantitative comparison with nature [*Ramberg*, 1981; *Weijermars and Schmeling*, 1986]. Analysis of modeling results and structural characteristics of fold-and-thrust belts suggests that both in nature and experiments the overall deformation style depends upon the rheology of the roof sequence-décollement system. The behavior of this brittle-ductile system can be described in terms of shear stress product ($\tau_b\tau_d$) and shear stress ratio (τ_b/τ_d), where τ_b and τ_d are the shear stress, calculated at the onset of deformation, at the base of the variably thick roof sequence and in the viscous layer, respectively.

[47] In a previous attempt, *Bonini* [2001] correlated products and ratios of the shear stresses in the models to natural fold belts and found a good correspondence between

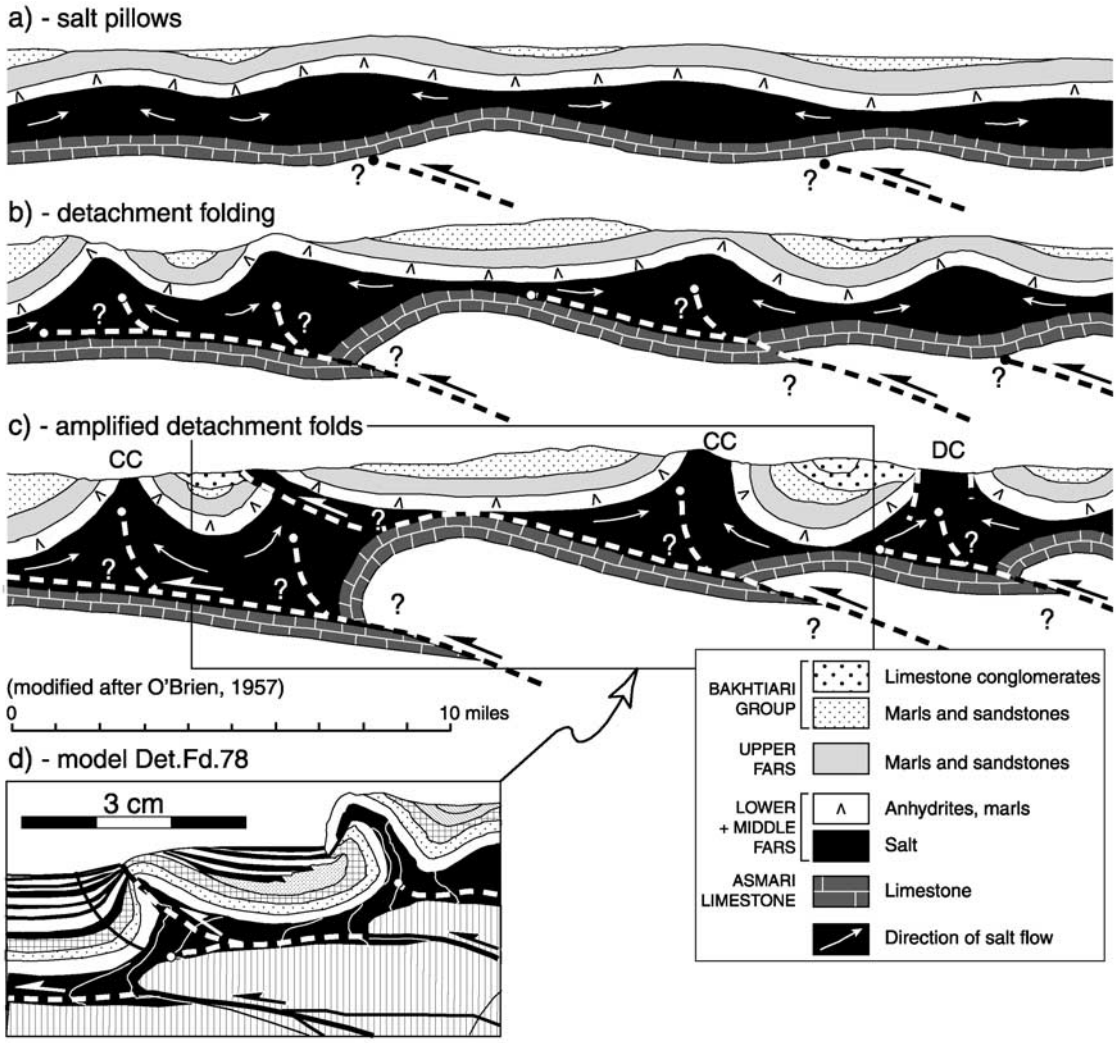

Figure 12. Cartoon showing the evolutionary path of detachment folds as inferred from deformation of the Fars salt in the Zagros fold-and-thrust belt (reprinted from *O'Brien* [1957, Figure 6], © Copyright 1957, with kind permission of Kluwer Academic Publishers). (a) Salt pillow stage, (b) detachment fold stage, (c) amplified, potentially diapiric, detachment fold stage (close of Upper Bakhtiari deposition). This evolution can be assumed as exemplifying that of detachment folds observed in the models, both with discordant (DC) and concordant (CC) contacts between the silicone and the overlying roof sequence (see Figure 7). Compare the patterns of detachment folds in Figure 12c with model Det.Fd.78 illustrated in Figure 12d. Notice the disharmony between the structures in the roof sequence and those in the floor sequence. The dashed line indicates the hypothetical position of thrust faults.

PRD or OFP deformation styles predicted by the modeling and those observed in the natural cases. Following this procedure, the experimental curve separating PRD and OFP domains in the models has been drawn by curvilinear (power law) regression using transition-style experimental data points (Figure 13a). The new experiments allow recalibration and better constraint of the previous empirical OFP-PRD transition curve reported in *Bonini* [2001] because of the addition of the weak décollement (type 1 models) includes much higher τ_b/τ_d ratios and lower $\tau_b\tau_d$ products than considered in the previous attempt. The numbers close to the regression curve in Figure 13a denote the models of series Det.Fd used to constrain the power law best fit, which gives:

$$y = 17652x^{-1.012}. \quad (6)$$

This curve is even closer to the Cartesian equation of equilateral hyperbola ($xy = a = const$) than the previous one, and the value $R \approx 1$ (see Figure 13a) indicates that this approximation is reliable. Modeling results have been compared, interpreted and extrapolated to natural conditions by plotting on a logarithmic diagram (Figure 13b) the experimental regression curve, scaled to natural conditions by transforming the shear stresses in the transition models

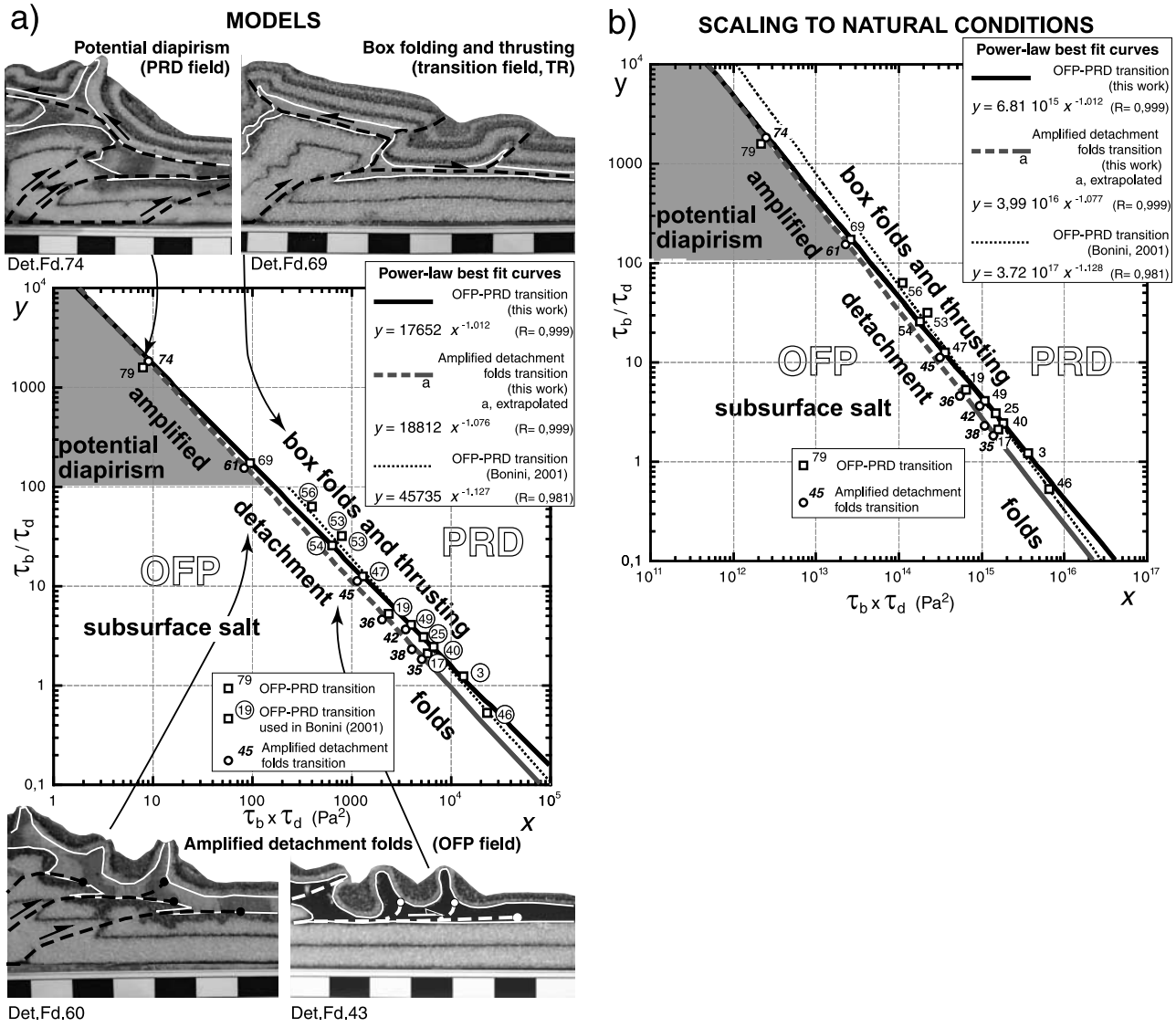

Figure 13. Best fit curves of amplified detachment folds and OFP-PRD transitions in (a) models and (b) scaled to nature. The curves are plotted on a logarithmic diagram with $x = \tau_b\tau_d$ and $y = \tau_b/\tau_d$ and are constrained by using transitional data points. On the basis of models results, the characteristics of the main deformation styles are schematically exemplified by insets in Figure 13a. The hypothesized area of potential salt diapirism is darkly shaded. OFP, outward fold propagation field; PRD, passive roof duplex field. See Table 2 and *Bonini* [2001] for model parameters. The thin white lines indicates the boundary of the silicone viscous layer; dashed lines indicate the inferred position of thrusts.

by the stress ratio $\sigma^* = \sigma_m/\sigma_n = 1.9\ 10^{-6}$ (Table 1), which is given as:

$$y = 6.81 \times 10^{15} x^{-1.012}. \quad (7)$$

Using the same procedure, from the experimental data points at the transition from amplified detachment folding to box folding and thrusting (see the exemplificative insets in Figure 13a) a power law best fit (with still $R \approx 1$; Figure 13a) gives:

$$y = 18812 x^{-1.076}, \quad (8)$$

while the corresponding curve scaled to nature (Figure 13b) is given as:

$$y = 3.99 \times 10^{16} x^{-1.077}, \quad (9)$$

which still indicates a nonlinear process with an equation close to the equilateral hyperbola. On the basis of the model results, the dark grey sector (enclosed between $\tau_b/\tau_d > 100$ and $\tau_b\tau_d < 100$ Pa^2 in model, and $\tau_b\tau_d < 3\ 10^{13}$ Pa^2 in nature) approximately indicates the field characterized by long-lived amplified detachment folds where the viscous material may potentially rise actively in the fold core

Table 3. Evaporite-Based Fold-and-Thrust Belts Parameters[a]

Fold-and-Thrust Belt	H_b, m	Estimated τ_b, Pa	H_d, m	Prevalent Décollement Lithology	Average Rate of Shortening, mm yr^{-1}	Estimated τ_d, Pa	H_b/H_d	Deformation Style and Occurrence of Diapiric Detachment Folds[c]	Reference Number in Figures 14 and B1
Appalachian Plateau (1)	~2000	4×10^7	~100	salt	5.0[b]	1.6×10^5	20	OFP, S (24)	1
Parry Islands (2)	5000	10^8	~500	salt	10.0 (2)	6.3×10^4	10	TR, N (2)	2
Eastern McKenzie (3)	~1800	3.6×10^7	200	salt	5.0[b]	7.9×10^4	9	OFP, U	3
Mississippi Fan (4)	~3300	6.6×10^7	500(?)	salt	5.0[b]	3.2×10^4	6.6	OFP, Y (4)	4
Eastern Cordillera (5)	~2800	5.6×10^7	~180	salt	~6.0 (19)	1.1×10^5	15.5	OFP, S (5)	5
Santos Basin (6)	~250	5×10^6	2000(?)	salt	5.0[b]	7.9×10^3	0.12	OFP, Y (6)	6
SE Pyrenees									
Serres Marginales (7)	~800	1.6×10^7	250	salt	4.6 (20)	5.8×10^4	3.2	OFP, Y(25)	7
Axial Zone (8)	~6000	1.2×10^8	~250	salt	4.6 (20)	5.8×10^4	24	PRD, N (8)	8
Jura (9)	1700	3.4×10^7	700	salt + anhyd.	2.5 (21)	1.1×10^4	2.4	OFP, N (9)	9
External N. Apennines (10)	~2400	4.8×10^7	1000	anhydrite	11.5 (10)	3.6×10^4	5	OFP, O (26)	10
Albanides (11)	~3000	6×10^7	~2000	salt	5.0[b]	7.9×10^3	2	OFP, S (11)	11
W. Hellenic Arc (12)	1500 (?)	3×10^7	~1500	salt	5.0[b]	10^4	1	OFP, Y (27)	12
Mediterranean Ridge (13)	~350	7×10^6	~1000	salt	40.0 (13)	1.3×10^5	0.35	OFP, N (28)	13
Eastern Rif (14)	~2500	5×10^7	~500	salt	~2.0 (22)	1.3×10^4	5	OFP, Y (14)	14
Zagros									
Fars Salt (15)	900	1.8×10^7	~1500	salt	26 (23)	5.5×10^4	0.6	OFP, Y (15)	15
Hormuz Salt (15)	6500	1.3×10^8	~1200	salt	26 (23)	6.8×10^4	5.4	OFP, O (15)	16
Salt Range (16)	~4000	8×10^7	~500	salt	11.5 (16)	7.3×10^4	8	TR, O (29)	17
W-Ural foredeep (17)	~2000	4×10^7	~800	salt	~10.0 (17)	3.9×10^4	2.5	OFP, Y (17)	18
Amadeus Basin (18)	~5000	10^8	~800	salt + anhyd.	5.0[b]	2×10^4	6.25	TR, Y (18)	19

[a]Thickness of roof sequences and décollement at the onset of deformation, as well as shortening rates and deformation characteristics are based on the following authors (numbers given in parentheses in columns 1, 6 and 9): 1, *Davis and Engelder* [1985]; 2, *Harrison* [1995a, 1995b]; 3, *Aitken and Long* [1978], *Davis and Engelder* [1985] and *Vann et al.* [1986]; 4, *Weimer and Buffler* [1992] and *Rowan* [1997]; 5, *McLaughlin* [1972]; 6, *Demercian et al.* [1993] and *Cobbold et al.* [1995]; 7, *Sans and Vergés* [1995]; 8, *Puigdefàbregas et al.* [1992]; 9, *Sommaruga* [1997]; 10, *Calamita* [1990] and *Calamita et al.* [1994]; 11, *Velaj et al.* [1999]; 12, *Underhill* [1988]; 13, *Ryan et al.* [1982] and *Chaumillon et al.* [1996]; 14, *Yovanovitch* [1922], *Burger et al.* [1962] and *Suter* [1980]; 15, *O'Brien* [1957] and *Colman-Sadd* [1978]; 16, *Baker et al.* [1988] and *Pennock et al.* [1989]; 17, *Artyushkov et al.* [2000]; 18, *Teyssier* [1985] and *Lindsay* [1987]; 19, *Jordan et al.* [1983]; 20, *Vergés et al.* [1996]; 21, *Pfiffner* [1986]; 22, *Morley* [1992]; 23, *Vita-Finzi* [1986]; 24, *Frey* [1973]; 25, *Sans and Koyi* [2001]; 26, *Andreozzi et al. 1987*; 27, *Brooks and Ferentinos* [1984], *Auroux et al.* [1984] and *Monopolis and Bruneton* [1982]; 28, *Costa and Vendeville* [2001]; 29, *Butler et al.* [1987]. The shear stress τ_b at the base of natural roof sequences is referred to the onset of shortening and has been calculated using the *Byerlee* [1968, 1978] criterion $\tau_b = \sigma\mu_b\ (1 - \lambda_b)$, with constants $\mu_b = 0.85$ and $c = 0$ MPa for depths lower than 10 km (or <200 MPa) [*Brace and Kohlstedt*, 1980; *Weijermars*, 1997; *Weijermars et al.*, 1993]. Values of τ_b are referred to dry conditions ($\lambda_b = 0$), while τ_d has been calculated using the Newton criterion (equation (3)) and it is referred to a mean salt viscosity $\eta = 10^{17}$ Pa s. In accord with experimental data by *Carter and Hansen* [1983], the estimated strength of salt is less than 1 MPa. An average volumetric mass $\rho_b = 2400$ kg m^{-3} has been assumed for sedimentary rocks of the roof sequence.

[b]A rate of 5 mm yr^{-1} has been assumed as mean rate of shortening for the computation of τ_d when natural rates were not available.

[c]OFP, outward fold propagation; PRD passive roof duplex; TR, transition style (both OFP and PRD). Occurrence of salt diapirism at detachment folds; Y, yes; N, no; S, suspect; U, unknown; O, other mechanisms of salt diapirism.

resulting in a ductile wall that may (or may not) exhibit disconformable contacts to the fold crest (see Figure 7) and rise out of the broken hinge (see insets in Figure 13a and Figure 8n).

[48] Plotting the shear stress ratios and products estimated (at the onset of deformation) for salt-based natural fold-and-thrust belts (Table 3) on a logarithmic diagram containing the scaled experimental regression curves, offers a practical method for comparing modeling results to natural conditions [*Bonini*, 2001]. Salt viscosity for specific décollement layers is rarely available, so that data points for particular fold belts have been plotted varying the salt viscosity from 10^{16} Pa s (Figure 14a) to 10^{19} Pa s (Figure 14b). The stress values computed for natural fold-and-thrust belts (for $\lambda_b = 0$) together with the correspondent deformation style (OFP, PRD or transition style, occurrence or absence of salt diapirism; Table 3) fit rather well the deformation fields predicted by the modeling (Figure 14), indicating a satisfactory correlation between the experimental results and the real natural cases. However, this comparison involves some limitations that need to be pointed out. The determination of H_b and H_d at the onset of shortening may represent a source of potential error in the shear stress estimates. The roof sequence thickness H_b can be influenced by uncertainties related to 1) the timing of onset of shortening, and to 2) the amount of erosion, while restoration of the initial décollement thickness H_d is affected by the flow of salt. In addition, diapirism may take place during late phases of shortening, when the geometry of tectonic thickening and syntectonic sediments may be very complex and highly variable across the thrust belt, thus complicating even more the determination of H_b. Another limitation concerns the fact that strain rates in nature have been simplistically determined at the onset of deformation assuming simple shear (see section 2.2 and Appendix A). As a final point, the transition curve has been built for amplified detachment folds that may possibly evolve to diapirs, while diapirism in fold-and-thrust belts may also develop according to other mechanisms

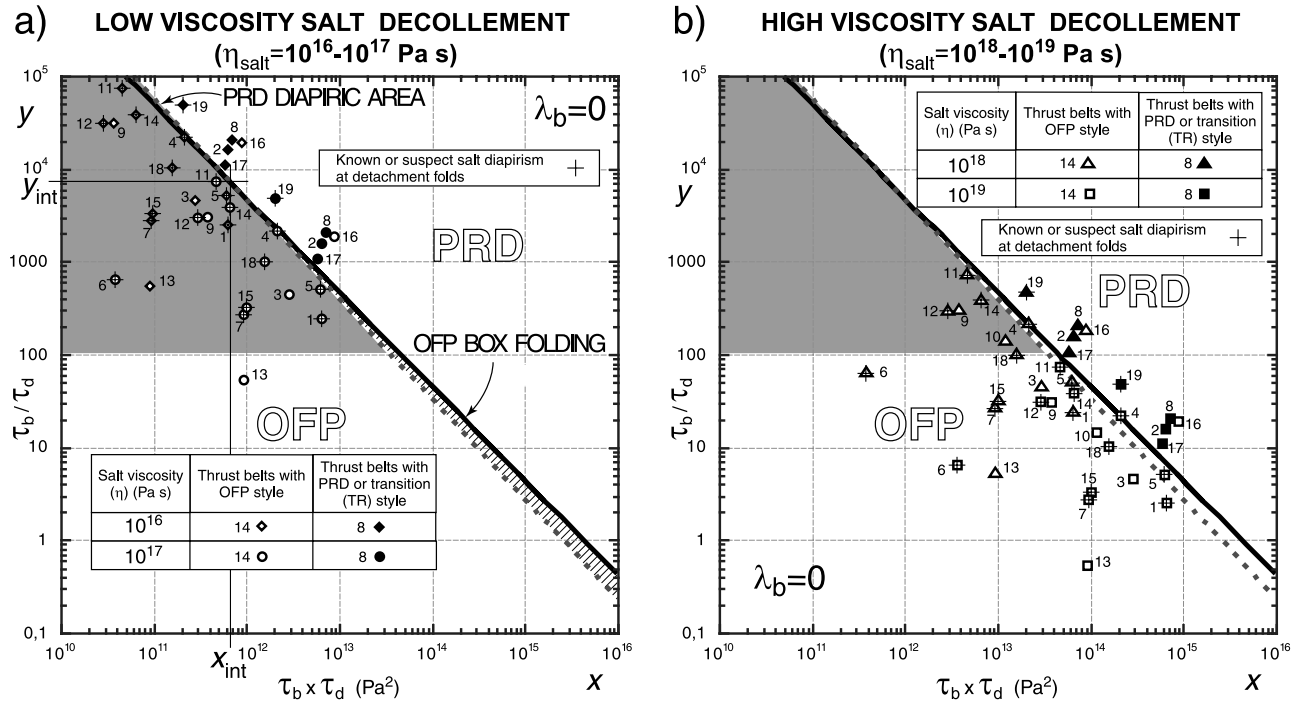

Figure 14. Shear stress products and ratios inferred for salt-based fold-and-thrust belts (Table 3) plotted on the scaled OFP-PRD and amplified detachment folds transition curves ($\lambda_b = 0$) considering (a) natural salt décollements with viscosity $\eta = 10^{16}$–10^{17} Pa s and (b) salt décollements with $\eta = 10^{18}$–10^{19} Pa s. Thrust belts with basal décollement composed of anhydrites (such as no. 10, External Northern Apennines) are plotted in Figure 14b only. Hatched area in Figure 14a indicates the sector in the OFP field, comprised between the two transition curves (equation (B12)), characterized by prevailing box folding without diapirism.

[e.g., *Cotton and Koyi*, 2000; *Vially et al.*, 1994; *Costa and Vendeville*, 2001], so that the comparison with nature might be not always straightforward.

[49] Analysis of Figure 14 suggests that for low salt viscosity ($\eta = 10^{16}$–10^{17} Pa s) fold-and-thrust belts falling in the OFP field should nearly all be characterized by conditions favorable to development of diapirism (Figure 14a). Conversely, increasing salt viscosity ($\eta = 10^{18}$–10^{19} Pa s) implies that almost all the OFP-style fold-and-thrust belts move outside the dark grey area (Figure 14b). This behavior may also suggest that natural detachment folds affecting thin roof sequences without salt piercement and salt at the surface might indicate the presence of a high-viscosity salt décollement.

[50] The experiments were performed in dry conditions ($\lambda = 0$), and the consideration of the more general case with finite pore fluid pressure is illustrated in detail in Appendix B, which shows the strong dependence of deformation styles transitions upon pore fluid pressure in the roof sequence (λ_b). Particularly, increasing the λ_b value reduces the brittle shear stress τ_b and the transition curves moves into the PRD field, giving increasing relevance to the OFP style. This behavior involves that chains exhibiting PRD style for $\lambda_b = 0$ may move into the OFP field, possibly also developing the conditions favourable to salt diapirism. In this view, alternate drops or increases in the fluid pressure may result in alternate phases dominated by PRD or OFP styles. This eventuality should be rather common and may explain why fold-and-thrust belts with relatively thick roof sequences (H_b = 4000–6500 m) are stable in the PRD field for $\lambda_b = 0$ and deform according to the OFP style, such as fold-and-thrust belts (indicated with TR in Table 3) 2 (Parry Island), 17 (Salt Range), and 19 (Amadeus Basin) (Figure 14 and Appendix B). Raised pore fluid pressure in the roof sequence could explain the dominant OFP style exhibited by the Zagros fold-and-thrust belt (data point 16) despite its great H_b thickness (see section 4.1.2).

[51] It is worth stressing here that OFP and PRD styles also depend upon increase in the roof sequence thickness H_b by synshortening sedimentation. This in turn implies that various structural styles may occur in different sectors and in different times during the evolution of a given thrust belt depending on the local H_b changes. Both end members (OFP and PRD) could coexist due to lateral variation in thickness that is typical of the syntectonic sedimentary wedges developing at the front of a growing fold-and-thrust belt, a setting favoring the development of OFP style in the foreland and PRD style in the hinterland. Taking the Northern Apennines as an example representative of many others, this fold-and-thrust belt (data point no. 10) began to deform with typical OFP style [e.g., *Calamita*, 1990; *Calamita et al.*, 1994]. Then, foredeep sedimentation, supplied from the Alps, doubled the roof sequence thickness (from 2400 up to more than 5000 m) so that PRD-like

structures developed in the hinterland while OFP deformation persisted in the most external sectors.

[52] As well as affecting the OFP-PRD transition, changes in pore fluid pressure in the roof sequence should also affect salt diapirism. An increase in pore fluid pressure weakens the roof sequence and widens the area of diapirism (Appendix B), and is expected to increase the critical thickness H_{bcrit} which can be potentially pierced by salt diapirs developing under conditions similar to the models. This supposition accords with the fact that modeling predicts (for $\lambda_b = 0$) a maximum H_{bcrit} of the order of 1200–1800 m (i.e., 4–6 mm in the model), but salt diapirs piercing detachment folds with roof sequences as thick as 3000 m have documented in nature (fold-and-thrust belts no. 4, 5, 11, and possibly 19; Table 3). Nevertheless, in nature, the roof sequence might be thinned by erosion at the anticline crest and favor diapirism, so that the actual H_{bcrit} might be significantly lower than the thickness of the roof sequence away from folds.

[53] In conclusion, the results discussed above highlight once more the importance of pore fluid pressure (λ_b) upon the development of fold-and-thrust belts [e.g., *Gretener*, 1981; *Cello and Nur*, 1988]. However, the tectonic scenarios in which synshortening salt diapirs may develop is rather complex and depend on a number of parameters that should be determined at the onset of (and possibly during) deformation. These include salt viscosity (η), roof sequence and salt décollement thickness (including synshortening sedimentation) (H_b, H_d), and pore fluid pressure (λ_b), though most of them are often poorly known. Despite these uncertainties, the relations between shear stresses and pore fluid pressure presented in this work may offer a tool for estimating quantitatively the tendency of a given fold-and-thrust belt to promote fold amplification and salt diapirism in detachment folds.

5. Concluding Remarks

[54] The above results illustrate the mechanical consistency of analogue models to be an effective tool for improving our understanding about the dynamics of tectonic processes. The main conclusions derived from this experimental work can be summarized as follows:

[55] 1. Analogue models confirm that, mostly depending upon the roof sequence strength, a shortened brittle-ductile system deforms according to two main geometric styles, outward fold propagation (OFP) and passive roof duplex (PRD), with shallow depth of burial favoring detachment folding (low H_b) and thick (or strong) roof sequences (high H_b) promoting PRD style.

[56] 2. Modeling results emphasize the importance of PRD structures in the deformation of thrust belts. Passive roof thrusts easily give rise to younger-over-older relations in contractional settings. This mechanism has apparently not received a sufficient attention so far although it is easy to confuse with low-angle normal faulting.

[57] 3. The viscosity of the décollement layer controls the horizontal propagation of detachment folding. which is higher for high-viscosity décollements (type 2 models) and practically nil for low-viscosity décollements (type 1 models). This may suggest that strong décollement layers may decouple structures in the roof sequence from those in floor sequence more effectively than a weak décollement layer.

[58] 4. The models show that the viscous layer flows from beneath the synclines and their flanks into the cores of anticlines in the roof sequence. In type 1 models, owing to the low τ_d, the deformation concentrates in a single long-lived detachment fold that amplifies significantly and typically exposes the ductile core at its crest. The rise of the viscous layer is intimately associated with strain localization above the tips of nominal ductile blind thrusts, and is accompanied by the development of a crestal graben which, depending on the relative activity of the fold limbs, may evolve to a dilatational fissure or be intruded by a ductile wall. In this latter case, the silicone intrudes the faults bounding the graben, rises above the broken fold hinge and may collapse over the surface.

[59] 5. Deformation patterns observed in the models can be qualitatively compared to those described for some natural examples of detachment folding compared with salt exposed locally along their cores, as in the northern Hellenic Arc and the Zagros.

[60] 6. Best fitting of experimental data points at the transition from (1) OFP to PRD and (2) from amplified detachment fold to box fold and thrusting indicates a nonlinear process with regression curves near to the equation for a Cartesian equilateral hyperbola ($y = ax^{-1}$). Comparison of the scaled transition curves with nature reveals a satisfactory correspondence between the deformation styles (OFP, PRD, TR, presence or absence of salt diapirism) predicted by the modeling and those reported in the literature for salt-based fold-and-thrust belts.

[61] 7. Scaling of models suggests that, in dry roof sequences, diapiric detachment folds in the OFP field may be quantitatively estimated to potentially occur in nature for $\tau_b/\tau_d > 100$ and $\tau_b\tau_d < 3\ 10^{13}$ Pa^2. Variations of pore fluid pressure in the roof sequence (λ_b) can shift the equilibrium field from PRD to OFP and vice versa during the lifetimes of particular fold-and-thrust belts. Increasing λ_b decreases the strength of a roof sequence that in turn should favor detachment folds to became active diapirs.

Appendix A: Deformation Patterns in Viscous Layers

[62] The final shapes of initially vertical strain markers vary through the silicone layer of type 1 models and demonstrates that the strain was heterogeneous [*Ramsay and Huber*, 1983]. For $H_b \geq 0.4$ cm (models Det.Fd.79, 74 and 76), the initially vertical passive markers in the silicone layer exhibit a markedly asymmetric distribution above the floor duplex. This distribution is consistent with a hinterlandward displacement of the roof sequence (PRD or transition styles; Figures 3b–3d). This effect is not observed in models with $H_b = 0.2$ cm (model Det.Fd.60) where most of the silicone was extruded vertically toward the core of small anticlines (OFP style; Figure 3a). Markers in the

silicone layer in front of the most external thrust fault in the floor sequence indicate either outward or inward flow (Figures 3a–3d). Here the silicone does not exhibit significant thickening, indicating that simple shear deformation represents a reasonable approximation for evaluating a strain rate in the model, which for simplicity has been calculated at the onset of shortening by equation (3) taking the initial H_d (see section 2.2).

[63] In a décollement layer composed of PDMS (type 2 models; see *Bonini* [2001]), the deformation pattern in front of the thrust fault in the floor sequence (T) still varies depending upon the deformation style of the roof sequence. In the PRD style, the initial circles and vertical markers in the viscous layer are still deformed roughly consistently with a simple shear deformation (Figure A1a; model Det.Fd.81 at 5% BS and H_b = 1 cm). The distortions of circles and vertical markers in OFP mode (Figure A1b) instead indicate a more complex deformation history, which combines pure and simple shear. In model Det.Fd.67 (5% BS and H_b = 0.2 cm;) the silicone exhibits a marked thickening, with strain markers outward (i.e., to the right) of fold 3 (but also inward of fold 1) indicating shortening by nearly pure shear (Figure A1b). A minor component of simple shear along the lower silicone boundary is suspected to occur inward of fold 3. Below folds 1–3 in the roof sequence, the upper boundary of the silicone PDMS is instead affected by mainly simple shear as a result of the relative outward displacement of the roof sequence in response to folding. This pattern might suggest that this simple shear deformation was superimposed onto the formerly pure shear-dominated deformation as folding progressed outward.

[64] Although strain in type 2 models with OFP style was heterogeneous, the strain rate might be still roughly approximated using equation (3). This because, for moderate percentages of bulk shortening, the horizontal and vertical velocities are similar. Considering the strain rate along the direction of the vertical axis u, it is given by the general equation for strain rate $\varepsilon = [(l_1 - l_o)/l_o]\, t^{-1}$, where l_1 and l_o are the final and initial length and t is the time of deformation. Strain rate along the vertical axis (u) can be written as:

$$\dot{\varepsilon}_u = \frac{\mathrm{d}u}{\mathrm{d}t\ u_o} = \frac{v_u}{u_o}, \qquad \text{(A1)}$$

where (calculating the strain rate at the onset of deformation) $u_o(= l_o) = H_d$. Assuming plain strain and area conservation, initial pure shear deformation (as exemplified by the ellipses to the right of fold 3 in Figure A1b), the initial strain marker circle deforms into an ellipse of equal area [e.g., *Price and Cosgrove*, 1990]:

$$(\text{circle area})\pi r^2 = ab\pi(\text{ellipse area}),$$

where, r is the radius of the initial circle, a and b are the minor and maximum semi axes of the ellipse, respectively (Figure A1c). During pure shear deformation, the semi axis

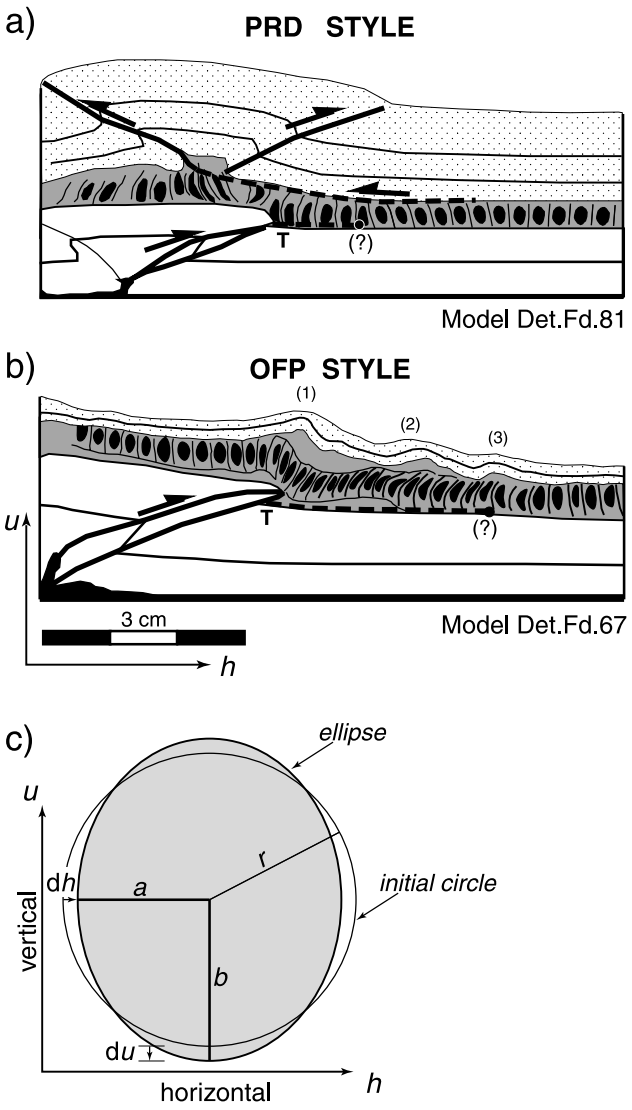

Figure A1. Deformation patterns in PDMS décollement (type 2) deduced by the distortion of initial circles placed vertically along a longitudinal section in the middle part of the viscous layer. Line drawings are of (a) model Det.Fd.81 (with PRD style) and (b) model Det.Fd.67 (with OFP style). In model Det.Fd.81, in front of the floor sequence thrust (T), the viscous layer reveals nearly simple shear deformation, which is given by the moving roof sequence detached above the décollement (along the passive roof thrust) with respect to the ''stationary'' floor sequence. In model Det.Fd.77, distortion of the strain markers circles suggests a more complex deformation pattern, with nearly simple shear superimposed onto early layer-parallel shortening (pure shear) deformation, which is suggested by the ellipses below the roof sequence unaffected by folding. (c) Parameters of pure shear deformation of an initial circle to an equal area ellipse for modest strain (approximately <10% bulk shortening).

a shortens by dh and, in the same time interval, the semi axis b lengthens by du (Figure A1c), so that:

$$a = r - \mathrm{d}h,$$

$$b = r + \mathrm{d}u.$$

Since $r^2 = ab$, then $r^2 = (r - \mathrm{d}h)(r + \mathrm{d}u)$, and resolving d$u$ in terms of dh we obtain:

$$\mathrm{d}u = \frac{r\,\mathrm{d}\,h}{r - \mathrm{d}\,h}, \tag{A2}$$

which, for an initial radius of unity becomes:

$$\mathrm{d}\,u = \frac{\mathrm{d}\,h}{1 - \mathrm{d}\,h}. \tag{A3}$$

From equation (A3), for modest strain (i.e., <10% bulk shortening) the contraction along axis h is very close to the lengthening along axis u, such that d$h \approx$ du is a reasonable approximation. This suggests that velocity components along axes h and u of the ellipses are similar and can be approximated as:

$$\left|\frac{\mathrm{d}\,h}{\mathrm{d}\,t}\right| \approx \left|\frac{\mathrm{d}\,u}{\mathrm{d}\,t}\right|, \text{ and } |v_h| \approx |v_u|.$$

Thus from equation (A1) it can be approximated (for low bulk shortening) that:

$$\dot{\varepsilon}_u = \dot{\varepsilon}_h \approx \dot{\gamma} = \frac{v_h}{H_\mathrm{d}}, \tag{A4}$$

which is the engineering strain rate given in equation (3). In the comparison of model results to nature, consideration of the engineering strain rate at the initial stages of shortening may be more practical than the geological horizontal strain rate because the viscous layer thickness may be estimated rather easily (e.g., from drills or stratigraphic sections), while estimation of the initial width requires the availability of more data sets (i.e., seismic sections as well as section restoration and balancing).

Appendix B: Deformation Styles, Salt Diapirism, and Pore Fluid Pressure (λ)

[65] The experiments were performed in dry conditions, thus with $\lambda = 0$. The analysis of the general case with finite pore fluid pressure in the roof sequence was considered in *Bonini* [2001]. That procedure is modified below by introducing the new power low best fit curves (equations 7 and 9 in section 4.2), the parameter cohesion, and correcting some inexactness contained in the previous equations. Starting from the Mohr-Coulomb equation for brittle failure:

$$\tau = \sigma\mu(1 - \lambda) + c, \tag{B1}$$

where τ and σ are the shear and normal stresses acting on the fault plane, $\mu = \tan\phi$ is the friction coefficient, ϕ is the angle of internal friction, λ is the Hubbert-Rubey coefficient of fluid pressure, and c is the cohesion, the coordinates of a generic point (x, y) in the diagrams of Figure 13 can be written as:

$$x = \tau_\mathrm{b}\tau_\mathrm{d} = [\sigma_\mathrm{b}\mu_\mathrm{b}(1 - \lambda_\mathrm{b}) + c_\mathrm{b}][\sigma_\mathrm{d}\mu_\mathrm{d}(1 - \lambda_\mathrm{d}) + c_\mathrm{d}],$$

$$y = \frac{\tau_\mathrm{b}}{\tau_\mathrm{d}} = \frac{[\sigma_\mathrm{b}\mu_\mathrm{b}(1 - \lambda_\mathrm{b}) + c_\mathrm{b}]}{[\sigma_\mathrm{d}\mu_\mathrm{d}(1 - \lambda_\mathrm{d}) + c_\mathrm{d}]},$$

where subscripts b and d refer to the roof sequence and the décollement layer composed of shale, respectively. Values of σ and μ can be considered constant, with $k = \sigma_\mathrm{b}\mu_\mathrm{b}$ and $k' = \sigma_\mathrm{d}\mu_\mathrm{d}$, so that:

$$x = kk'[(1 - \lambda_\mathrm{b}) + (c_\mathrm{b}/k)][(1 - \lambda_\mathrm{d}) + (c_\mathrm{d}/k')],$$

$$y = \frac{k[(1 - \lambda_\mathrm{b}) + (c_\mathrm{b}/k)]}{k'[(1 - \lambda_d) + (c_\mathrm{d}/k')]},$$

and, considering $Y = \dfrac{k}{k'}$ and $X = kk'$, this reduces to:

$$\begin{aligned} x &= X[(1 - \lambda_\mathrm{b}) + (c_\mathrm{b}/k)][(1 - \lambda_\mathrm{d}) + (c_\mathrm{d}/k')], \\ y &= Y\frac{[(1 - \lambda_b) + (c_b/k)]}{[(1 - \lambda_d) + (c_\mathrm{d}/k')]}. \end{aligned} \tag{B2}$$

Substituting equations (B2) in equation (7) it gives:

$$Y = [(1 - \lambda_\mathrm{b}) + (c_\mathrm{b}/k)]^{-2.012}[(1 - \lambda_\mathrm{d}) + (c_\mathrm{d}/k')]^{-0.012}AX^{-1.012}, \tag{B3}$$

where $A = 6.81 \times 10^{15}$ Pa$^{2.024}$. Considering the *Byerlee* [1968, 1978] criterion for depths <10 km (or <200 MPa), which is appropriate for roof sequences, $\mu_\mathrm{b} = 0.85$ and $c_\mathrm{b} = 0$ [*Brace and Kohlstedt*, 1980; *Weijermars*, 1997]. In the case of a shale décollement $\mu_\mathrm{d} = 0.25$ above 5.5 km depth, $\mu_\mathrm{d} = 0.55$ between 5.5 and 11 km and $\mu_\mathrm{d} = 0.7$ below 11 km; $c_\mathrm{d} = 0$ above 11 km and $c_\mathrm{d} = 25$ MPa below [*Weijermars et al.*, 1993]. Therefore in the range of the sedimentary cover (depths $\leq$10 km) cohesion can be considered as negligible ($c_\mathrm{b} = 0$ and $c_\mathrm{d} = 0$), so that:

$$Y = (1 - \lambda_\mathrm{b})^{-2.012}(1 - \lambda_\mathrm{d})^{-0.012}AX^{-1.012}. \tag{B4}$$

Nevertheless, this paper focuses on salt décollement where $\tau_\mathrm{d} = \eta\varepsilon$, so that equation (B4) reduces to:

$$Y_{trans} = (1 - \lambda_\mathrm{b})^{-2.012}AX^{-1.012}, \tag{B5}$$

where subscript *trans* refers to OFP-PRD transition in salt-based fold-and-thrust belts. Notably, equations (B4) and (B5) correct the corresponding equations in *Bonini* [2001] where the sign of the exponents was incorrectly reported as positive. This mistake involved some erroneous conclusions

concerning the shifting of the OFP-PRD transition because of its dependence upon pore fluid pressure. Therefore the procedure for evaluating a priori the tendency of a given roof sequence-décollement system to develop OFR or PRD styles described in *Bonini* [2001] is still valid but it should be partly modified taking into account these new equations.

[66] Applying to the transition form amplified detachment folds to box folds and thrusting in nature the procedure outlined above, from equation (9) this boundary can be expressed as:

$$Y = [(1 - \lambda_b) + (c_b/k)]^{-2.077}\,[(1 - \lambda_d) + (c_d/k')]^{-0.077} BX^{-1.077}, \tag{B6}$$

where $B = 3.99 \times 10^{16}$ Pa$^{2.144}$. Then, for salt décollements, equation (B6) reduces to:

$$Y_{ampl} = (1 - \lambda_b)^{-2.077} BX^{-1.077}, \tag{B7}$$

where subscript *ampl* refers to the transition to amplified detachment folds developing in salt-based fold-and-thrust belts. The dependence of deformation styles transition curves (equations B5 and B7) on pore fluid pressure is plotted on Figure B1a for $\lambda_b = 0$, $\lambda_b = 0.4$, $\lambda_b = 0.7$ and $\lambda_b = 0.9$, showing the progressive shifting of the transition curves into the PRD field.

[67] The relations between the various structural styles exhibited by fold-and-trust belts can be also evaluated considering both the intersection and the area between the experimental curves at OFP-PRD and amplified detachment folds transitions. The intersection point can be computed solving the system composed of equations (B3) and (B6):

$$\begin{cases} Y = D^{-0.012} E^{-2.012} AX^{-1.012} \\ Y = D^{-0.077} E^{-2.077} BX^{-1.077} \end{cases}, \tag{B8}$$

where $D = (1 - \lambda_d) + (c_d/k')$, $E = (1 - \lambda_b) + (c_b/k)$. Substituting the Y value of the lower equation into the upper equation of the system yields:

$$X^{0.065} = BA^{-1} D^{-0.065} E^{-0.065}.$$

After rearranging the equations, the coordinates of the generic intersection point can be expressed as:

$$\begin{cases} X = (BA^{-1})^{(1/0.065)} (DE)^{-1} & \text{(B9)} \\ Y = A^{(1.077/0.065)} B^{-(1.012/0.065)} DE^{-1} & \text{(B10)} \end{cases}$$

The position of the intersection point (x_{int}, y_{int}) between the two transition curves (see for instance those in Figures 14a and B1a calculated by equations B9 and B10) implies that there is a region in the OFP field characterized by prevailing box folding without diapirism and another smaller region in the PRD field where diapirism might be potentially

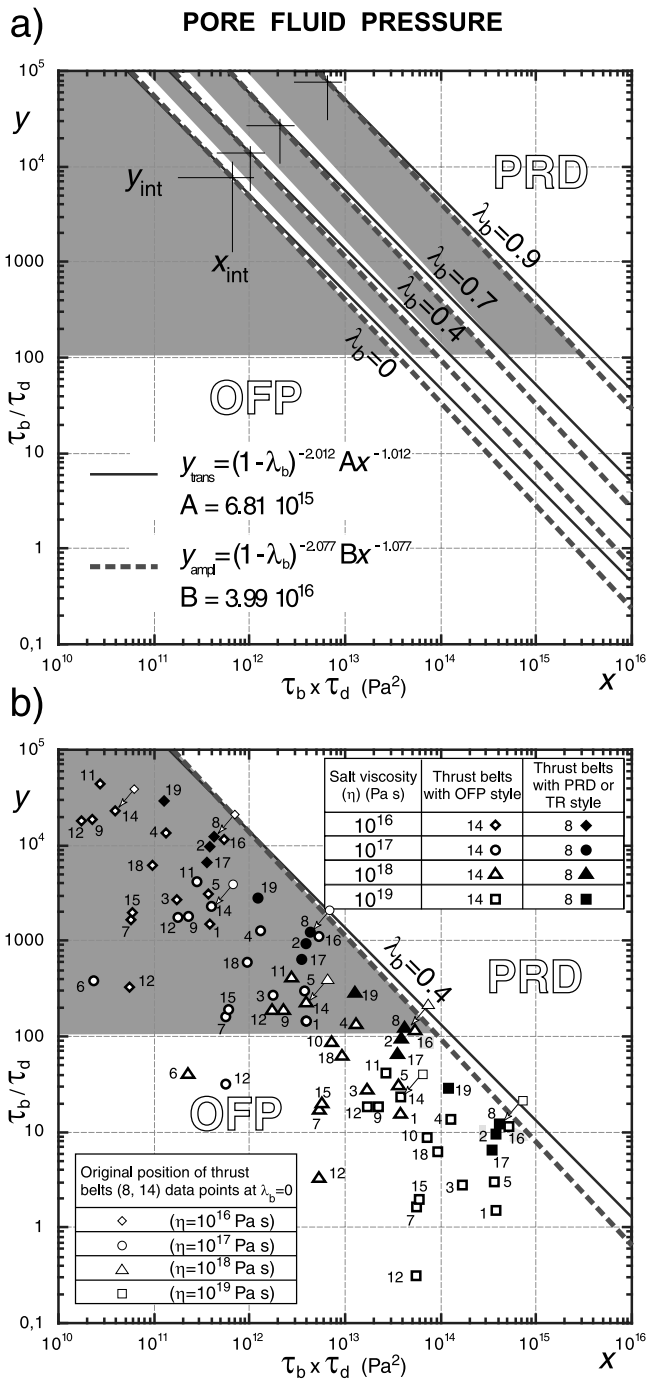

Figure B1. (a) Diagram showing the dependence of OFP-PRD and amplified detachment folding–box folding transitions upon pore fluid pressure in the roof sequence λ_b. The OFP-PRD transition curves correct those in *Bonini* [2001]. The box folding area in the OFP field comprised between the transition curve pair increases with λ_b. (b) Shifting of fold-and-thrust belts data points calculated for various salt viscosities and in case of $\lambda_b = 0.4$. Note that all data points move into the OFP area. The white arrows indicate the shifting of data points 8 and 14 (chosen as representative) from $\lambda_b = 0$ to $\lambda_b = 0.4$.

promoted. Salt diapirism at the front of the Peruvian Andes described by *Vann et al.* [1986], as well as the deformation of the Gardiner Range Thrust at the margin of the Amadeus Basin reported in *Lindsay* [1987], might perhaps be examples of diapirism at detachment folds associated with PRD style (compare with model Det.Fd.74 in Figure 3c and model Det.Fd.66 in Figures 8m and 8n).

[68] The area included between the two transition curves in the OFP field with prevailing box folding without diapirism (hatched area in Figure 14a) is also depending on λ_b. Such an area can be obtained analytically by integrating the difference between equations (B3) and (B6):

$$Area = \int_a^b \left[\left(D^{-0.012}E^{-2.012}AX^{-1.012}\right) - \left(D^{-0.077}E^{-2.077}BX^{-1.077}\right)\right]dx, \tag{B11}$$

which, for facilitating the computation, can be simplified by introducing $Kost_1 = D^{-0.012}E^{-2.012}A$, and $Kost_2 = D^{-0.077}E^{-2.077}B$, thus becoming:

$$Area = \int_a^b \left[\left(Kost_1X^{-(1012/1000)}\right) - \left(Kost_2X^{-(1077/1000)}\right)\right]dx.$$

Solving the integral, the generic equation for the area between the two transition curves can be expressed as:

$$Area = Kost_1\frac{10^3}{12}\left(a^{-0.012} - b^{-0.012}\right) + Kost_2\frac{10^3}{77}\left(b^{-0.077} - a^{-0.077}\right), \tag{B12}$$

where a and b are the integration boundaries. From Figure B1a, it appears that the intersection point (x_{int}, y_{int}) is clearly dependent upon λ_b. Taking boundary a as the intersection point x_{int} (determined from equation B9 for the various values of λ_b) and boundary b conveniently fixed at 10^{15} Pa^2, implies that the box folding area in the OFF field depends upon λ_b and, for the λ_b values considered in Figure B1a, it is maximum for $\lambda_b = 0.9$. Nevertheless, even at $\lambda_b = 0.4$ all the data points representing natural fold-and-thrust belts are shifted into the OFP field (see Figure B1b), suggesting that PRD and transition style (TR) data points may fall into the area (in the OFP field) contained between the two transition curves (as well as into the fields of PRD and PRD with potential diapirism) only in case of pore fluid pressure conditions with $\lambda_b < 0.4$. In such a case, depending on both salt viscosity and λ_b, part of PRD and TR chains with salt décollement with viscosities of the order of 10^{16}–10^{17} Pa s move into the dark grey area in the OFP, while some of those with high salt viscosity ($\eta \approx 10^{18}$–10^{19} Pa s, but also some of those with $\eta = 10^{17}$ Pa s) move into the OFP area without diapirism (subsurface salt) (see for instance the trajectories indicating the shifting of thrust belts data points 8 and 14 from $\lambda_b = 0$ to $\lambda_b = 0.4$ in Figure B1b). These considerations might be also used for constraining rough estimates of the décollement viscosities in natural brittle-ductile systems by comparing the inferred shear stresses and the characteristics of salt diapirism with the deformation fields predicted considering λ_b. Obviously, the behavior illustrated in Figure B1 represents only an incomplete and simplified view of reality. Thus pore fluid pressure may vary through the roof sequence in either/both space or time [e.g., *Cobbold et al.*, 2001]. The value of pore fluid pressure that can be measured in boreholes is instantaneous on the scale of thrust belt development and might be not realistic for the whole time span in which the fold-and-thrust belt has been developing. Remarkably, this observation raises the possibility that, during its evolution, a given fold-and-thrust may migrate from PRD to OFP, as well as from diapiric to nondiapiric fields, and vice versa.

[69] **Acknowledgments.** The constructive and careful revision of the manuscript by C. Talbot, an anonymous reviewer, and the Associate Editors O. Oncken and F. Roure helped to clarify several points. The paper has greatly benefited from the fruitful discussions with G. Corti, M. Poneti, and C. Tanini. Research granted by ordinary funds of CNR, Institute of Geosciences and Earth Resources (IGG) and by Università degli Studi di Firenze, Fondi di Ricerca d'Ateneo 2002 (responsible F. Sani).

References

Acocella, V., F. Salvini, R. Funiciello, and C. Faccenna, The role of transfer structures on volcanic activity at Campi Flegrei (southern Italy), *J. Volcanol. Geotherm. Res.*, *91*, 123–139, 1999.

Aitken, J. D., and D. G. F. Long, Mackenzie tectonic arc: Reflection of early basin configuration?, *Geology*, *6*, 626–629, 1978.

Ala, M. A., Salt diapirism in southern Iran, *AAPG Bull.*, *58*, 1758–1770, 1974.

Andreozzi, M., S. Casanova, S. Chicchi, S. Ferrari, P. E. Patterlini, M. Pesci, and G. Zanzucchi, Riflessione sulle evaporiti triassiche dell'alta Val Secchia (RE), *Mem. Soc. Geol. Ital.*, *39*, 69–75, 1987.

Arenas, C., H. Millán, G. Pardo, and A. Pocoví, Ebro Basin continental sedimentation associated with late compressional Pyrenean tectonics (north-eastern Iberia): Controls on basin margin fans and fluvial systems, *Basin Res.*, *13*, 65–89, 2001.

Artyushkov, E. V., M. A. Baer, P. A. Chekhovich, and N.-A. Mörner, The southern Urals. Decoupled evolution of the thrust belt and its foreland: A consequence of metamorphism and lithospheric weakening, *Tectonophysics*, *320*, 271–310, 2000.

Auroux, C., J. Mascle, and S. Rossi, Geologia del margine Ionico delle isole Strofadi a Corfù (estremità settentrionale dell'Arco Ellenico), *Mem. Soc. Geol. Ital.*, *27*, 267–286, 1984.

Baker, D. M., R. J. Lillie, R. S. Yeats, G. D. Johnson, M. Yousuf, and A. S. Hamid Zamin, Development of the Himalayan frontal thrust zone: Salt Range, Pakistan, *Geology*, *16*, 3–7, 1988.

Banks, C. J., and J. Warburton, "Passive-roof" duplex geometry in the frontal structures of the Kirthar and Sulaiman mountain belts, Pakistan, *J. Struct. Geol.*, *8*, 229–237, 1986.

Beloussov, V. V., Types of folding and their origin, *Intl. Geol. Rev.*, *1*, 1–21, 1959.

Berberian, M., Master "blind" thrust faults hidden under the Zagros folds: Active basement tectonics and surface morphotectonics, *Tectonophysics*, *241*, 193–224, 1995.

Blay, P., J. W. Cosgrove, and J. M. Summers, An experimental investigation of the development of structures in multilayers under the influence of gravity, *J. Geol. Soc. London*, *133*, 329–342, 1977.

Bonini, M., Passive roof thrusting and forelandward fold propagation in scaled brittle-ductile physical models of thrust wedges, *J. Geophys. Res.*, *106*, 2291–2311, 2001. (Correction, *J. Geophys. Res., 106*, 8955, 2001.)

Brace, W. F., and D. L. Kohlstedt, Limits on lithospheric stress imposed by laboratory experiments, *J. Geophys. Res.*, *85*, 6248–6252, 1980.

Brooks, M., and G. Ferentinos, Tectonics and sedimentation in the Gulf of Corinth and the Zakynthos and Kefallinia Channels, western Greece, *Tectonophysics*, *101*, 25–54, 1984.

Brun, J.-P., Narrow rifts versus wide rifts: Inferences for the mechanics of rifting from laboratory experiments, *Philos. Trans. R. Soc. London*, *357*, 695–712, 1999.

Brun, J.-P., and T. Nalpas, Graben inversion in nature and experiments, *Tectonics*, *15*, 677–687, 1996.

Burg, J.-P., P. Davy, and J. Martinod, Shortening of analogue models of the continental lithosphere: New hypothesis for the formation of the Tibetan plateau, *Tectonics*, *13*, 475–483, 1994.

Burger, J. J., B. Housse, and R. Lévy, Contribution des travaux d'exploration de la Société Chérifienne des Pétroles a la connaissance de la Nappe Prérifaine, in *Livre a la Memoire de P. Fallot*, vol. 1, pp. 423–430, Soc. Geol. de Fr., Paris, 1962.

Butler, R. W. H., M. P. Coward, G. M. Harwood, and R. J. Knipe, Salt control on thrust geometry, structural style and gravitational collapse along the Himalayan Mountain Front in the Salt Range of Northern Pakistan, in *Dynamical Geology of Salt and Related Structures*, edited by I. Lerche and J. J. O'Brien, pp. 339–418, Academic, San Diego, Calif., 1987.

Byerlee, J. D., Brittle-ductile transition in rocks, *J. Geophys. Res.*, *73*, 4741–4750, 1968.

Byerlee, J. D., Friction of rocks, *Pure Appl. Geophys.*, *116*, 615–626, 1978.

Calamita, F., Thrusts and fold-related structures in the Umbria-Marche Apennines (central Italy), *Ann. Tectonicae*, *4*, 83–117, 1990.

Calamita, F., G. Cello, G. Delana, and W. Paltrineri, Structural styles, chronology rates of deformation, and time-space relationships in the Umbria-Marche thrust system (central Apennines, Italy), *Tectonics*, *13*, 873–881, 1994.

Carter, N. L., and F. D. Hansen, Creep of rocksalt, *Tectonophysics*, *92*, 275–333, 1983.

Cello, G., and A. Nur, Emplacement of foreland thrust systems, *Tectonics*, *7*, 261–271, 1988.

Chaumillon, E., J. Mascle, and H. J. Hoffmann, Deformation of the western Mediterranean Ridge: Importance of Messinian evaporitic formations, *Tectonophysics*, *263*, 163–190, 1996.

Cobbold, P. R., P. Davy, D. Gapais, E. A. Rossello, E. Sadybakasov, J. C. Thomas, J. J. Tondji Biyo, and M. de Urreiztieta, Sedimentary basins and crustal thickening, *Sediment. Geol.*, *86*, 77–89, 1993.

Cobbold, P. R., D. Coelho, P. Szatmari, L. S. Demercian, and E. A. Rossello, Seismic and experimental evidence for thin-skinned horizontal shortening by convergent radial gliding on evaporites, Deep-water Santos Basin, Brazil, *AAPG Mem.*, *65*, 305–321, 1995.

Cobbold, P. R., S. Durand, and R. Mourgues, Sandbox modelling of thrust wedges with fluid-assisted detachments, *Tectonophysics*, *334*, 245–258, 2001.

Colletta, B., J. Letouzey, R. Pinedo, J. F. Ballard, and P. Balé, Computerized X ray tomography analysis of sandbox models: Examples of thin-skinned thrust systems, *Geology*, *19*, 1063–1067, 1991.

Collyer, A. A., Time independent fluids, *Phys. Educ.*, *8*, 333–338, 1973.

Colman-Sadd, S. P., Fold development in Zagros Simply Folded Belt, southwest Iran, *AAPG Bull.*, *62*, 984–1003, 1978.

Costa, E., and B. Vendeville, Diapirism in convergent settings triggered by hinterland pinch-out of viscous decollement: A hypothesis from modeling, *Geol. Soc. Am. Mem.*, *193*, 123–130, 2001.

Cotton, J. T., and K. A. Koyi, Modeling of thrust fronts above ductile and frictional detachments: Application to structures in the Salt Range and Potwar Plateau, Pakistan, *Geol. Soc. Am. Bull.*, *112*, 351–363, 2000.

Davis, D. M., and T. Engelder, The role of salt in fold-and-thrust belts, *Tectonophysics*, *119*, 67–88, 1985.

Davis, D. M., J. Suppe, and F. A. Dahlen, Mechanics of fold-and-thrust belts and accretionary wedges, *J. Geophys. Res.*, *88*, 1153–1172, 1983.

Davison, I., M. Insley, M. Harper, P. Weston, D. Blundell, K. McClay, and A. Quallington, Physical modelling of overburden deformation around salt diapirs, *Tectonophysics*, *228*, 255–274, 1993.

Davy, P., and P. R. Cobbold, Experiments on shortening of a 4-layer model of the continental lithosphere, *Tectonophysics*, *188*, 1–25, 1991.

DeCelles, P., M. B. Gray, K. D. Ridgway, R. B. Cole, P. Srivastava, N. Pequera, and D. A. Pivnik, Kinematic history of a foreland uplift from Paleocene synorogenic conglomerate, Beartooth Range, Wyoming and Montana, *Geol. Soc. Am. Bull.*, *103*, 1458–1475, 1991.

Delaney, P. T., D. D. Pollard, J. I. Ziony, and E. H. McKee, Field relations between dikes and joints: Emplacement processes and paleostress analysis, *J. Geophys. Res.*, *91*, 4920–4938, 1986.

Demercian, S., P. Szatmari, and P. R. Cobbold, Style and pattern of salt diapirs due to thin-skinned gravitational gliding, Campos and Santos basins, offshore Brazil, *Tectonophysics*, *228*, 393–433, 1993.

Dixon, J. M., Finite strain and progressive deformation in models of diapiric structures, *Tectonophysics*, *28*, 89–124, 1975.

Edgell, H. S., Salt tectonism in the Persian Gulf Basin, *Spec. Publ. Geol. Soc. London*, *100*, 129–151, 1996.

Faccenna, C., D. Giardini, P. Davy, and A. Argentieri, Initiation of subduction at Atlantic-type margins: Insights from laboratory experiments, *J. Geophys. Res.*, *104*, 2749–2766, 1999.

Farhoudi, G., A comparison of Zagros geology to island arcs, *J. Geol.*, *86*, 323–334, 1978.

Ford, M., E. A. Williams, A. Artoni, J. Vergés, and S. Hardy, Progressive evolution of a fault-related fold pair from growth strata geometries, Sant Llorenç de Morunys, SE Pyrenees, *J. Struct. Geol.*, *19*, 413–441, 1997.

Frey, M. G., Influence of Salina Salt on structure in New York-Pennsylvania part of Appalachian Plateau, *AAPG Bull.*, *57*, 1027–1037, 1973.

Gordy, P. L., F. R. Frey, and D. K. Norris (Eds.), *Geological Guide for the Canadian Society of Petroleum Geologists and 1977 Waterton-Glacier Park Field Conference*, 93 pp., Can. Soc. of Petrol. Geol., Calgary, Alberta, Canada, 1977.

Gretener, P. E., Pore pressure, discontinuities, isostasy and overthrust, *Spec. Publ. Geol. Soc. London*, *9*, 33–39, 1981.

Gutscher, M.-A., N. Kukowski, J. Malavieille, and S. Lallemand, Episodic imbricate thrusting and underthrusting: Analog experiments and mechanical analysis applied to the Alaskan Accretionary Wedge, *J. Geophys. Res.*, *103*, 10,161–10,176, 1998.

Harrison, J. C., Tectonics and kinematics of a foreland folded belt influenced by salt, Arctic Canada, *AAPG Mem.*, *65*, 379–412, 1995a.

Harrison, J. C., Melville Island's salt-based fold belt, Arctic Canada, *Bull. Geol. Surv. Can.*, *472*, 331 pp., 1995b.

Hessami, K., Tectonic history and present day deformation in the Zagros fold-thrust belt, Ph.D. thesis, Acta Univ. Upsaliensis, Uppsala, Sweden, 2002.

Homza, T. X., and W. K. Wallace, Geometric and kinematic models for detachment folds with fixed and variable detachment depths, *J. Struct. Geol.*, *17*, 575–588, 1995.

Hubbert, M. K., Theory of scale models as applied to the study of geologic structures, *Geol. Soc. Am. Bull.*, *48*, 1459–1520, 1937.

Jackson, M. P. A., and C. J. Talbot, External shapes, strain rates, and dynamics of salt structures, *Geol. Soc. Am. Bull.*, *97*, 305–323, 1986.

Jackson, M. P. A., and C. J. Talbot, Advances in salt tectonics, in *Continental Deformation*, edited by P. L. Hancock, pp. 159–179, Pergamon, New York, 1994.

Jackson, M. P. A., and B. C. Vendeville, Regional extension as a geologic trigger for diapirism, *Geol. Soc. Am. Bull.*, *106*, 57–73, 1994.

Jaeger, J. C., and N. G. W. Cook, *Fundamentals of Rock Mechanics*, 3rd ed., 593 pp., Chapman and Hall, New York, 1979.

Jamison, W. R., Geometric analysis of fold development in overthrust terranes, *J. Struct. Geol.*, *9*, 207–219, 1987.

Jordan, T. E., B. L. Isacks, R. W. Allmendinger, J. A. Brewer, V. A. Ramos, and C. J. Ando, Andean tectonics related to geometry of subducted Nazca plate, *Geol. Soc. Am. Bull.*, *94*, 341–361, 1983.

Kent, P. E., The salt plugs of the Persian Gulf region, *Trans. Leicester Lit. Philos. Soc.*, *64*, 56–88, 1970.

Koyi, H., Experimental modeling of role of gravity and lateral shortening in Zagros mountain belt, *AAPG Bull.*, *72*, 1381–1394, 1988.

Koyi, H. A., K. Hessami, and A. Teixell, Epicenter distribution and magnitude of earthquakes in fold-thrust belts: Insights from sandbox models, *Geophys. Res. Lett.*, *27*, 273–276, 2000.

Lindsay, J. F., Upper Proterozoic evaporites in the Amadeus basin, central Australia, and their role in basin tectonics, *Geol. Soc. Am. Bull.*, *99*, 852–865, 1987.

Liu, H., K. McClay, and D. Powell, Physical models of thrust wedges, in *Thrust Tectonics*, edited by K. R. McClay, pp. 71–81, Chapman and Hall, New York, 1992.

Malavieille, J., Modélisation expérimentale des chevauchements imbriqués: Application aux chaînes de montagnes, *Bull. Soc. Geol. Fr.*, *26*, 129–138, 1984.

Martinod, J., and P. Davy, Periodic instabilities during compression of the lithosphere: 2. Analogue experiments, *J. Geophys. Res.*, *99*, 12,057–12,069, 1994.

McClay, K. R., Glossary of thrust tectonics terms, in *Thrust Tectonics*, edited by K. R. McClay, pp. 419–433, Chapman and Hall, New York, 1992.

McLaughlin, D. H., Evaporite deposits of Bogotà area, Cordillera Oriental, Colombia, *AAPG Bull.*, *56*, 2240–2259, 1972.

Meigs, A. J., Sequential development of selected Pyrenean thrust faults, *J. Struct. Geol.*, *19*, 481–502, 1997.

Millán, H., M. Aurell, and A. Melendez, Synchronous detachment folds and coeval sedimentation in the Prepyrenean External Sierras (Spain): A case study for the tectonic origin of sequences and systems tracts, *Sedimentology*, *41*, 1001–1024, 1994.

Millán, H., A. Pocoví, and A. Casas, El frente de cabalgamiento surpirenaico en el extremo occidental de las Sierras Exteriores: Sistemas imbricados y pliegues de despegue, *Rev. Soc. Geol. Esp.*, *8*, 73–91, 1995.

Monopolis, D., and A. Bruneton, Ionian Sea (western Greece): Its structural outline deduced from drilling and geophysical data, *Tectonophysics*, *83*, 227–242, 1982.

Morley, C. K., Tectonic and sedimentary evidence for synchronous and out-of-sequence thrusting, Larache-Acilah area, western Moroccan Rif, *J. Geol. Soc. London*, *149*, 39–49, 1992.

Mulugeta, G., Modelling the geometry of Coulomb thrust wedges, *J. Struct. Geol.*, *10*, 847–859, 1988.

Mulugeta, G., and H. Koyi, Three-dimensional geometry and kinematics of experimental piggyback thrusting, *Geology*, *15*, 1052–1056, 1987.

Nalpas, T., and J.-P. Brun, Salt flow and diapirism related to extension at crustal scale, *Tectonophysics*, *228*, 349–362, 1993.

Nilsen, K. T., B. C. Vendeville, and J.-T. Johansen, Influence of regional tectonics on halokinesis in the Nordkapp Basin, Barents Sea, *AAPG Mem.*, *65*, 413–436, 1995.

O'Brien, C. A. E., Salt diapirism in South Persia, *Geol. Mijnbouw*, *19*, 357–376, 1957.

Pennock, E. S., R. J. Lillie, A. S. H. Zaman, and M. Yousaf, Structural interpretation of seismic

reflection data from eastern Salt Range and Potwar Plateau, Pakistan, *AAPG Bull.*, *73*, 841–857, 1989.
Pfiffner, O. A., Evolution of the north Alpine foreland basin in the central Alps, *Spec. Publ. Int. Assoc. Sedimentol.*, *8*, 219–228, 1986.
Poblet, J., and S. Hardy, Reverse modelling of detachment fold: Application to the Pico del Aguila anticline in the south central Pyrenees (Spain), *J. Struct. Geol.*, *17*, 1707–1724, 1995.
Poblet, J., and K. McClay, Geometry and kinematics of single-layer detachment folds, *AAPG Bull.*, *80*, 1085–1109, 1996.
Poblet, J., K. McClay, F. Storti, and J. A. Munoz, Geometries of syntectonic sediments associated with single-layer detachment folds, *J. Struct. Geol.*, *19*, 369–381, 1997.
Poliakov, A. N. B., R. Van Balen, Y. Y. Podladchikov, B. Daudre, S. Cloetingh, and C. J. Talbot, Numerical analysis of how sedimentation and redistribution of surficial sediments affects salt diapirism, *Tectonophysics*, *226*, 199–216, 1993.
Poliakov, A. N. B., Y. Y. Podladchikov, E. C. Dawson, and C. J. Talbot, Salt diapirism with simultaneous brittle faulting and viscous flow, *Spec. Publ. Geol. Soc. London*, *100*, 291–302, 1996.
Price, N. J., and J. W. Cosgrove, *Analysis of Geological Structures*, 502 pp., Cambridge Univ. Press, New York, 1990.
Price, R. A., The Cordilleran foreland thrust and fold belt in the southern Canadian Rocky Mountains, *Spec. Publ. Geol. Soc. London*, *9*, 427–448, 1981.
Puigdefàbregas, C., J. A. Muñoz, and J. Vergés, Thrusting and foreland basin evolution in the southern Pyrenees, in *Thrust Tectonics*, edited by K. R. McClay, pp. 247–254, Chapman and Hall, New York, 1992.
Ramberg, H., *Gravity, Deformation and Earth's Crust*, 452 pp., Academic, San Diego, Calif., 1981.
Ramsay, J. G., and M. I. Huber, *The Techniques of Modern Structural Geology*, vol. 1, *Strain Analysis*, 307 pp., Academic, San Diego, Calif., 1983.
Riba, O., Syntectonic unconformities of the Alto Cardener, Spanish Pyrenees: A genetic interpretation, *Sediment. Geol.*, *15*, 213–233, 1976.
Rowan, M. G., Three-dimensional geometry and evolution of a segmented detachment fold, Mississippi Fan foldbelt, Gulf of Mexico, *J. Struct. Geol.*, *19*, 463–480, 1997.
Ryan, W. B. F., K. A. Kastens, and M. B. Cita, Geological evidence concerning compressional tectonics in the eastern Mediterranean, *Tectonophysics*, *86*, 213–242, 1982.
Sans, M., and H. A. Koyi, Modeling the role of erosion in diapir development in contractional settings, *Geol. Soc. Am. Mem.*, *193*, 111–122, 2001.
Sans, M., and J. Vergés, Fold development related to contractional salt tectonics: Southeastern Pyrenean thrust front, Spain, *AAPG Mem.*, *65*, 369–378, 1995.
Sans, M., A. L. Sánchez, and P. Santanach, Internal structure of a detachment horizon in the most external part of the Pyrenean fold and thrust belt (northern Spain), *Spec. Publ. Geol. Soc. London*, *100*, 65–76, 1996.
Schultz-Ela, D. D., M. P. A. Jackson, and B. C. Vendeville, Mechanics of active salt diapirism, *Tectonophysics*, *228*, 275–312, 1993.
Schwerdtner, W. M., Identification of evaporite diapirs formed under the influence of horizontal compression, *Bull. Can. Petrol. Geol.*, *34*, 271–276, 1986.
Sokoutis, D., M. Bonini, S. Medvedev, M. Boccaletti, C. J. Talbot, and H. Koyi, Indentation of a continent with a built-in thickness change: Experiment and nature, *Tectonophysics*, *320*, 243–270, 2000.
Sommaruga, A., Geology of the central Jura and the Molasse Basin: New insight into an evaporite-based foreland fold and thrust belt, *Mem. 12*, 176 pp., Soc. Neuchâteloise des Sci. Nat., Neuchâtel, Switzerland, 1997.
Storti, F., and K. McClay, Influence of syntectonic sedimentation on thrust wedges in analogue models, *Geology*, *23*, 999–1002, 1995.
Storti, F., F. Salvini, and K. McClay, Fault-related folding in sandbox analogue models of thrust wedges, *J. Struct. Geol.*, *19*, 583–602, 1997.
Storti, F., F. Salvini, and K. McClay, Synchronous and velocity-partitioned thrusting and thrust polarity reversal in experimentally produced, doubly-vergent thrust wedges: Implications for natural orogens, *Tectonics*, *19*, 378–396, 2000.
Suppe, J., G. T. Chou, and S. C. Hook, Rates of folding and faulting determined from growth strata, in *Thrust Tectonics*, edited by K. R. McClay, pp. 105–121, Chapman and Hall, New York, 1992.
Suppe, J., F. Sàbat, J. A. Muñoz, J. Poblet, E. Roca, and J. Vergés, Bed-by-bed fold growth by kink-band migration: Sant Llorenç de Morunys, eastern Pyrenees, *J. Struct. Geol.*, *19*, 443–461, 1997.
Suter, G., Carte structurale de la Chaine Rifaîne, *Map 245b*, scale 1:500,000, Geol. Surv. Morocco, Rabat, 1980.
Talbot, C. J., and M. Alavi, The past of a future syntaxis across the Zagros, *Spec. Publ. Geol. Soc. London*, *100*, 89–109, 1996.
Talbot, C. J., H. Koyi, D. Sokoutis, and G. Mulugeta, Identification of evaporite diapirs formed under the influence of horizontal compression: A discussion, *Bull. Can. Petrol. Geol.*, *36*, 91–95, 1988.
Talbot, C. J., S. Medvedev, M. Alavi, H. Shahrivar, and E. Heidari, Salt extrusion at Kuh-e-Jahani, Iran: June 1994 to November 1997, *Spec. Publ. Geol. Soc. London*, *174*, 93–110, 2000.
Tavarnelli, E., Evidence for fault-propagation folding in the Umbria-Marche-Sabina Apennines (central Italy), *Ann. Tectonicae*, *7*, 87–99, 1993.
Ten Grotenhuis, S. M., S. Piazolo, T. Pakula, C. W. Passchier, and P. D. Bons, Are polymers suitable rock analogs?, *Tectonophysics*, *350*, 35–47, 2002.
Teyssier, C., A crustal thrusts system in an intracratonic tectonic environment, *J. Struct. Geol.*, *7*, 689–700, 1985.
Turner, J. P., and P. L. Hancock, Relationships between thrusting and joint systems in the Jaca thrust-top basin, Spanish Pyrenees, *J. Struct. Geol.*, *12*, 217–226, 1990.
Underhill, J. R., Triassic evaporites and Plio-Quaternary diapirism in western Greece, *J. Geol. Soc. London*, *145*, 269–282, 1988.
Van Keken, P. E., C. J. Spiers, A. P. Berg, and E. J. Muysert, The effective viscosity of rocksalt: Implementation of steady-state creep laws in numerical models of salt diapirism, *Tectonophysics*, *225*, 457–476, 1993.
Vann, I. R., R. H. Graham, and A. B. Hayward, The structure of mountain fronts, *J. Struct. Geol.*, *8*, 215–227, 1986.
Velaj, T., I. Davison, A. Serjani, and I. Alsop, Thrust tectonics and the role of evaporites in the Ionian Zone of the Albanides, *AAPG Bull.*, *83*, 1408–1425, 1999.
Vendeville, B. C., Thin-skinned compressional structures above frictional plastic and viscous décollement layers, *Geol. Soc. Am. Abstr. Prog.*, *23*(5), A423, 1991.
Vendeville, B. C., and M. P. A. Jackson, Critical roof thickness of active diapirs, *Eos Trans. AGU*, *73*(43), Fall Meet. Suppl., 572, 1992a.
Vendeville, B. C., and M. P. A. Jackson, The rise of diapirs during thin-skinned extension, *Mar. Petrol. Geol.*, *9*, 331–353, 1992b.
Vergés, J., D. W. Burbank, and A. Meigs, Unfolding: An inverse approach to fold kinematics, *Geology*, *24*, 175–178, 1996.
Vially, R., J. Letouzey, F. Bernard, N. Haddadi, G. Deforges, H. Askri, and A. Boudjema, Basin inversion along the North African margin: The Sahara Atlas (Algeria), in *Peri-Tethyan Platforms*, edited by F. Roure, pp. 79–118, Technip, Paris, 1994.
Vita-Finzi, C., *Recent Earth Movements: An Introduction to Neotectonics*, 226 pp., Academic, San Diego, Calif., 1986.
Weijermars, R., Flow behaviour and physical chemistry of bouncing putties and related polymers in view of tectonic laboratory applications, *Tectonophysics*, *124*, 325–358, 1986.
Weijermars, R., *Principles of Rock Mechanics*, 359 pp., Alboran Sci., Amsterdam, 1997.
Weijermars, R., and H. Schmeling, Scaling of Newtonian and non-Newtonian fluid dynamics without inertia for quantitative modelling of rock flow due to gravity (including the concept of rheological similarity), *Phys. Earth Planet. Inter.*, *43*, 316–330, 1986.
Weijermars, R., M. P. A. Jackson, and B. Vendeville, Rheological and tectonic modeling of salt provinces, *Tectonophysics*, *217*, 143–174, 1993.
Weimer, P., and R. T. Buffler, Structural geology and evolution of the Mississippi Fan fold belt, deep Gulf of Mexico, *AAPG Bull.*, *76*, 225–251, 1992.
Yovanovitch, B., La géologie du pétrole au Maroc, *Bull. Soc. Geol. Fr.*, *22*, 234–245, 1922.
Zapata, T. R., and R. W. Allmendinger, Growth stratal records of instantaneous and progressive limb rotation in the Precordillera thrust belt and Bermejo basin, Argentina, *Tectonics*, *15*, 1065–1083, 1996.

M. Bonini, Istituto di Geoscienze e Georisorse, Sezione di Firenze, Consiglio Nazionale delle Ricerche, via G. La Pira 4, I-50121, Firenze, Italy. (mbonini@geo.unifi.it)

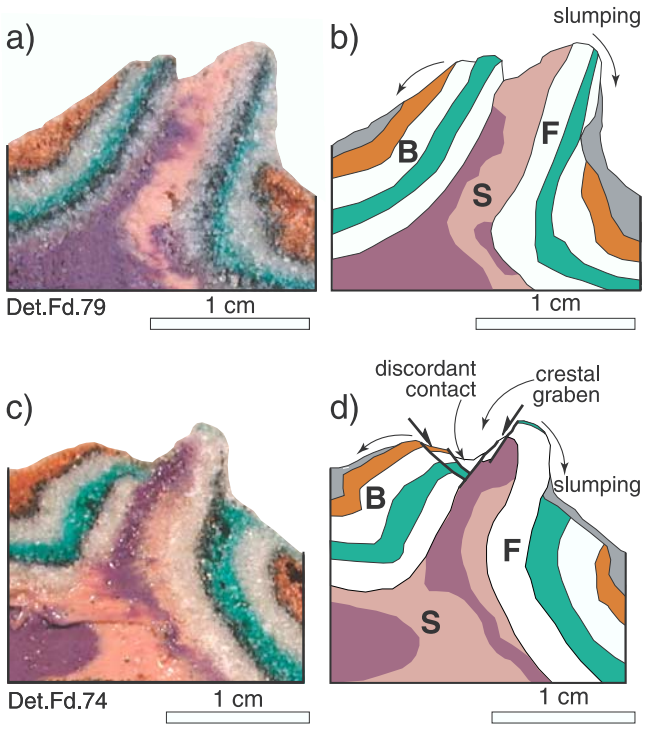

Figure 6. Close-up of detachment fold cores exemplifying the two main deformation patterns identified in type 1 models. (a) Photograph and (b) interpretative line drawing of a ductile wall exhibiting concordant contacts with both fold limbs. Note the sense of asymmetry of the top silicone free surface at the fold core pointing to a faster growth rate of the forelimb. (c) Photograph and (d) interpretative line drawing of a ductile wall exhibiting a disconformable contact with the broken fold hinge. B, backlimb; F, forelimb; S, silicone.

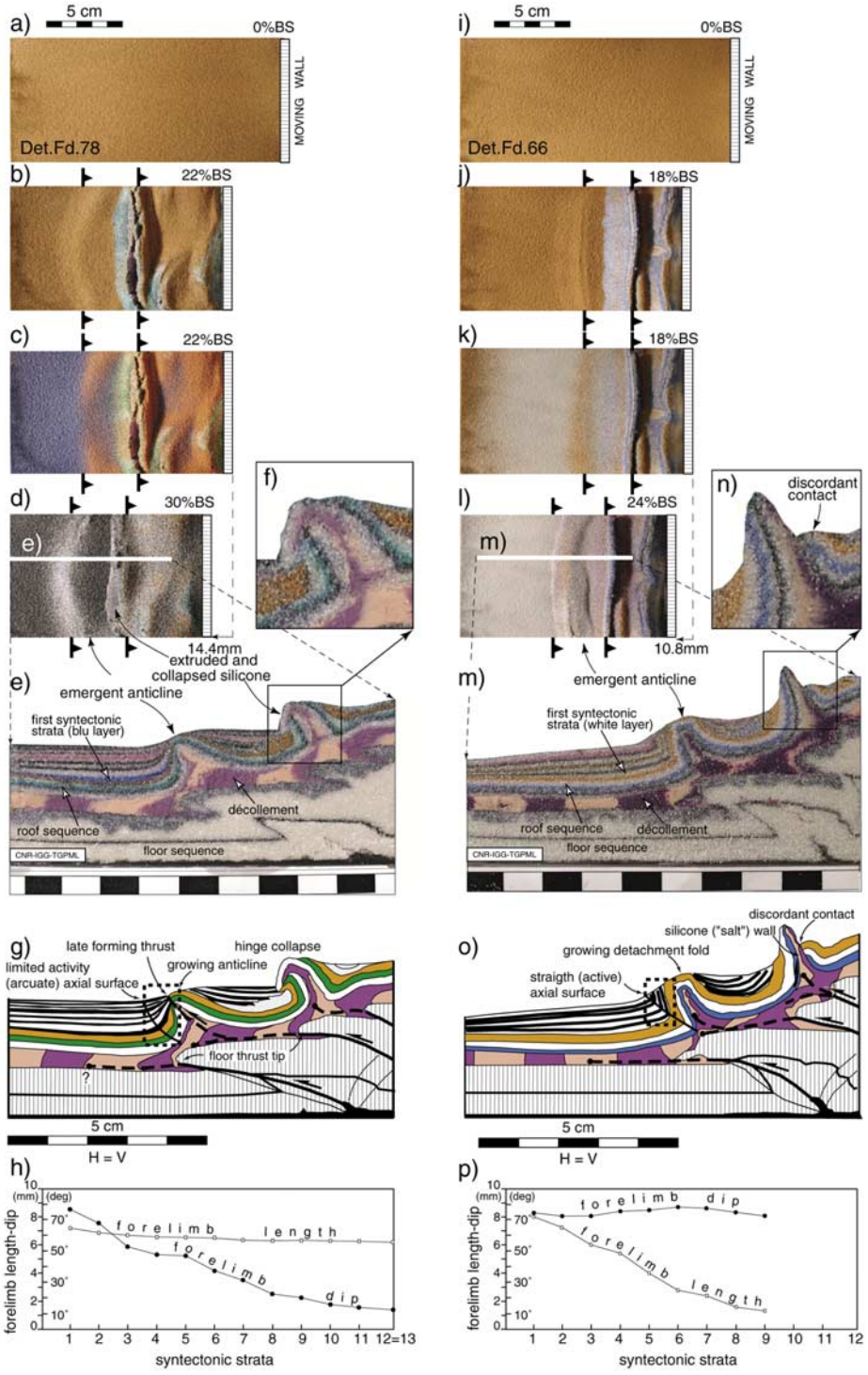

Figure 8. Models performed with synshortening sedimentation. Top view photographs illustrate the main experimental phases: (a, i) initial, (b, j) prior to sedimentation, (c, k) after the first sedimentation event, and (d, l) final topography. (e, m) Transversal sections and (g, o) corresponding line drawings show detachment folds located typically above floor thrusts tips. The black box in Figures 8e and 8m indicates the close-up of amplified detachment folds in Figures 8f and 8n. The dashed box in Figures 8g and 8o at the frontal part of the emergent anticline indicates were dip and length of syntectonic strata have been measured and reported in the diagrams of Figures 8h and 8p. Numbers in Figures 8h and 8p denote the growth strata from the lower to the upper. Black triangles indicate the position of the main blind floor thrusts tip.